J. Mech. Phys. Solids 196 (2025) 106018

Contents lists available at ScienceDirect

Journal of the Mechanics and Physics of Solids

journal homepage: www.elsevier.com/locate/jmps

Multimaterial topology optimization of elastoplastic composite structures

Yingqi Jia [a], Weichen Li [a], Xiaojia Shelly Zhang [a,b,c,*]

[a] Department of Civil and Environmental Engineering, University of Illinois Urbana-Champaign, Urbana, IL 61801, USA
[b] Department of Mechanical Science and Engineering, University of Illinois Urbana-Champaign, Urbana, IL 61801, USA
[c] National Center for Supercomputing Applications, Urbana, IL 61801, USA

ARTICLE INFO

Keywords:
Plasticity
Topology optimization
Multimaterial
J2-flow
Delayed yielding
Energy dissipation

ABSTRACT

Plasticity is indispensable for wide-ranging structures as a protection mechanism against extreme loads. Tailoring elastoplastic behaviors such as stiffness, yield force, and energy dissipation to optimal states is therefore crucial for safety and economics. Recent studies have optimized either geometry or material phase for desired energy dissipating capacities; however, integrating both in design optimization is essential but thus far not achieved, impeding a comprehensive understanding of the interplay among structural geometry, material heterogeneity, and plasticity. Here, we propose a general topology optimization framework for discovering lightweight, multimaterial structures with optimized elastoplastic responses under small deformations. This framework features a multiobjective optimization formulation that simultaneously enhances initial stiffness, delays plastic yielding, and maximizes energy absorption/dissipation. The approach is built upon rigorous elastoplasticity theory and the celebrated return mapping algorithm, incorporating both isotropic and kinematic hardening. We analytically derive the history-dependent sensitivities using the reversed adjoint method and automatic differentiation. Employing the proposed framework, we investigate several composite structures and demonstrate the non-intuitive optimized geometries and material distributions that deliver diverse superior elastoplastic performances, including maximized plastic energy dissipation and various degrees of yield resistance. Furthermore, our findings reveal underlying mechanisms that enhance structural elastoplastic performance, such as leveraging sequential yielding to prolong post-yielding resistance and prevent catastrophic failure. These optimized designs and discovered mechanisms reveal the principles for creating the next generation of resilient engineering structures accounting for elastoplastic behaviors.

1. Introduction

Plastic behavior is ubiquitous among engineering materials such as metals, plastics, and soils, and has shaped the design principles of structures in mechanical (Prager, 1955), civil (Zhang et al., 2018; Jia et al., 2022), and aerospace (Gupta et al., 2015) engineering. While plasticity is generally not preferred under normal operating conditions for some applications, it is crucial for structural safety under extreme loading. Examples include the dissipation of seismic energy in buildings through the yielding of steel dampers (Zhang et al., 2018; Jia et al., 2022) and the crash protection of automobiles enabled by plastic buckling of bumpers (Jia et al., 2021). Despite its significance, the plastic behavior of structures is still primarily designed in a qualitative, experience-based, and relatively

* Corresponding author at: Department of Civil and Environmental Engineering, University of Illinois Urbana-Champaign, Urbana, IL 61801, USA.
E-mail address: zhangxs@illinois.edu (X.S. Zhang).

https://doi.org/10.1016/j.jmps.2024.106018
Received 14 July 2024; Received in revised form 29 September 2024; Accepted 20 December 2024
Available online 1 January 2025

restrictive manner. Such practices rarely elucidate the influence of geometry and material variation on structural plastic responses, nor do they harness these factors to improve plastic performance. In contrast, topology optimization (Bendsøe and Kikuchi, 1988; Bendsoe and Sigmund, 2003; Wang et al., 2021), a computational morphogenesis approach, has the potential to optimize structural elastoplastic behaviors as it has been successfully tailored to achieve programmable responses (Li et al., 2022, 2023; Jia et al., 2024b,a,c) and enhanced failure resistance (Jia et al., 2023).

Advancement has been made in integrating topology optimization with plasticity. Existing studies typically focus on optimizing either structural geometries with a single material (Maute et al., 1998; Wallin et al., 2016; Alberdi and Khandelwal, 2017; Amir, 2017; Li et al., 2017; Alberdi and Khandelwal, 2019b; Kim and Yun, 2020; Ivarsson et al., 2021; Abueidda et al., 2021; Boissier et al., 2021; Desai et al., 2021; Zhang et al., 2023) or material phases without varying geometry (Nakshatrala and Tortorelli, 2015; Alberdi and Khandelwal, 2019a; Li et al., 2021). Given the significant influence of both the geometry and the material phases on the structural plastic behavior, the lack of a comprehensive investigation of their interaction may obscure important mechanisms dependent on both factors. This gap also prevents the discovery of new optimized multimaterial patterns that could offer superior elastoplastic performance.

In addition to focusing on the optimization of either the geometries or the material phases, the field has mainly explored designing for single-objective functions. For instance, Zhang et al. (2023) minimize the material volume fraction of elastoplastic structures under a yielding constraint. Desai et al. (2021) maximize the total compliance of structures while imposing a material volume constraint. Li et al. (2021) maximize the end force of designs, also subject to a material volume constraint. These studies have successfully derived optimized structures for a single design objective. The interplay between various design objectives and different elastoplastic behaviors remains underexplored. Unifying diverse objectives and constraints in a multiobjective framework can provide a more comprehensive design tool, expand design freedom, and potentially yield more robust performance by balancing various critical elastoplastic behaviors. This approach also offers an avenue for understanding the interplay among different elastoplastic responses.

In this study, we propose multimaterial and multiobjective topology optimization to create composite metallic structures with optimized elastoplastic responses and elucidate various geometric and material mechanisms for enhancing desired elastoplastic performance. The main research concept is depicted in Fig. 1. For a given design domain, we seek to identify the geometry and distribution of multiple metallic materials with dissimilar elastoplastic properties that optimize the combination of sufficient initial stiffness, delayed yielding, and maximized energy.

To achieve the goals, we need to address two challenges: simulating elastoplasticity and computing strongly history-dependent sensitivities (Fig. 1(b)). To accurately simulate structural elastoplastic responses, we adopt the well-established J_2-flow plasticity theory equipped with the return mapping scheme (Simo and Hughes, 2006), incorporating both isotropic and kinematic hardening for completeness. To evaluate the complex history-dependent sensitivities, we leverage the combined use of the reversed adjoint method (Alberdi et al., 2018) and automatic differentiation (Margossian, 2019). The reversed adjoint method captures the history dependency of elastoplasticity by recursively computing the sensitivities from the last to the first load step. Automatic differentiation effortlessly evaluates the partial derivatives involved in the adjoint method, eliminating tedious chain rule calculations. Once these challenges are addressed, we can evaluate the structural elastoplastic responses based on the design variables and compute the sensitivities from these structural responses. This treatment forms a closed-loop topology optimization framework (Fig. 1(a)–(b)) that iteratively updates the design variables until convergence, ultimately achieving the target elastoplastic responses.

Based on this topology optimization framework, we obtain composite structures with diverse optimized elastoplastic performance as illustrated in Fig. 1(c), including delayed yielding and maximized total energy with sufficient initial stiffness, by which the optimized structure significantly outperforms the reference maximized stiffness design. Through the optimized designs in this work, we discover multiple mechanical mechanisms for improving structural elastoplastic responses. For example, in a metallic damper design, although the stronger material may not yield, it transmits higher loads to the weaker material, thereby indirectly increasing the energy dissipation of the entire system. Additionally, these optimized dampers exhibit high stiffness for small applied displacements and demonstrate a high peak force for large applied displacements, as energy dissipation is proportional to the peak force. Moreover, through the design of yield-resistant structures, we uncover a parallel arrangement of distinct materials that features sequential material yielding. This arrangement decouples structural yielding from material yielding, thus preventing catastrophic failure. We also show that delayed yielding is achieved by altering load paths and enhancing total energy is accomplished by distributed plastic regions.

The remainder of this paper is organized as follows. Section 2 briefly reviews the fundamentals of elastoplasticity theories under small deformations, providing the state equations used in the proposed topology optimization framework outlined in Section 3. Following this, we present three sample case studies in Section 4 to showcase the optimized structures with enhanced elastoplastic performance and the underlying mechanisms. Finally, Section 5 offers several concluding remarks. The paper is complemented by three appendices. Appendix A details the history-dependent sensitivity analysis based on the reversed adjoint method and automatic differentiation, where we also present sensitivity verification. Appendix B introduces the conversion from design variables to physical variables. Appendix C compares the elastoplastic responses of optimized designs defined on voxel-based and body-fitted meshes.

2. Small-deformation elastoplasticity: theory and numerical implementation

In this section, we briefly review the J_2-flow theory under small deformations (Simo and Hughes, 2006), which is used to predict structural elastoplastic responses and support the development of the subsequent topology optimization in Section 3. To implement this plasticity theory, we also recap the return mapping algorithm and provide a solution scheme for finite element analysis (FEA). The details of the J_2-flow theory, the return mapping algorithm, and the FEA solution scheme are outlined below.

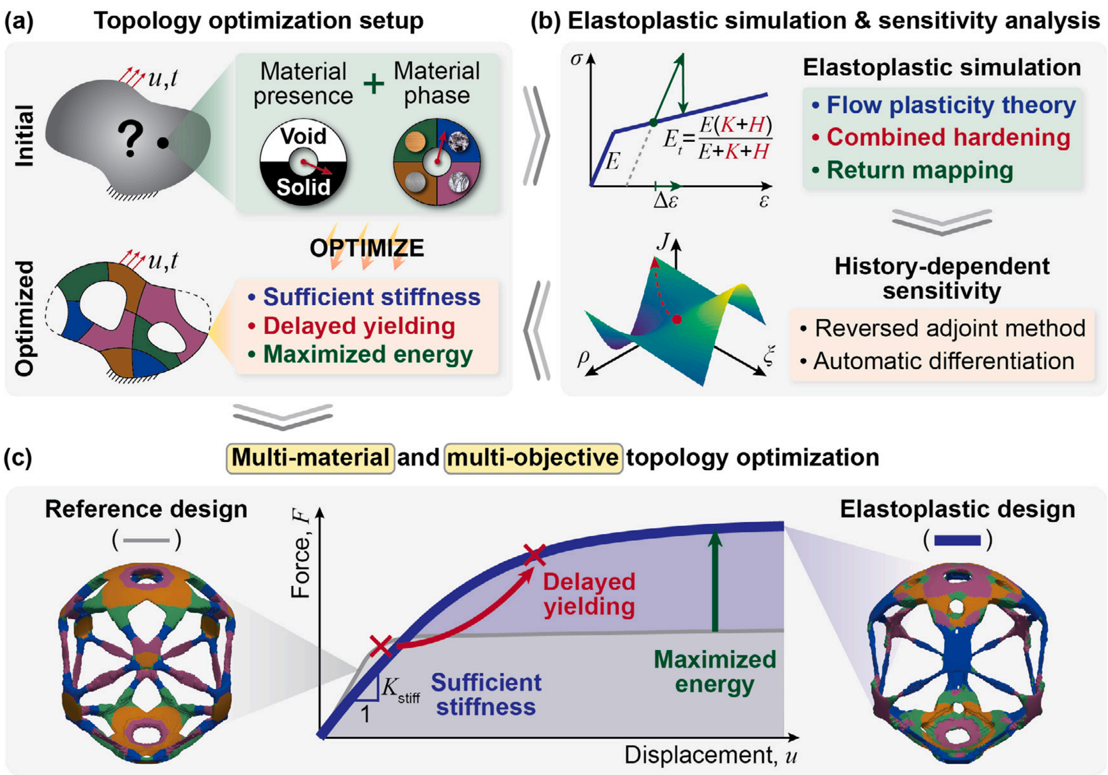

Fig. 1. Multimaterial and multiobjective topology optimization for designing elastoplastic structures. (a) Topology optimization setup. The variables u and t represent the applied displacement and traction loading amplitudes, respectively. (b) Elastoplastic simulation and sensitivity analysis. The variables σ and ε are the uniaxial stress and strain, respectively. The variable E is the Young's modulus, and E_t is the elastoplastic modulus. The variables K and H are the isotropic and kinematic hardening moduli, respectively. The variable $\Delta\varepsilon$ is the incremental strain. The variable J represents a general function of interest. The design variables ρ and ξ describe the material presence and phase in (a), respectively. (c) Multimaterial and multiobjective topology optimization. The variable $K_{\mathtt{stiff}}$ is the initial structural stiffness.

2.1. J_2-Flow plasticity theory

In this subsection, we recap the J_2-flow plasticity theory (Simo and Hughes, 2006) used to predict the structural elastoplastic responses. Specifically, we consider an open bounded design domain, Ω, subjected to quasi-static displacement loading, $\bar{\mathbf{u}}(t)$, on one part of the boundary, $\partial\Omega_D$, and traction loading, $\bar{\mathbf{t}}(t)$, on the complementary boundary, $\partial\Omega_{\mathcal{N}}$, such that $\partial\Omega = \overline{\partial\Omega_D \cup \partial\Omega_{\mathcal{N}}}$, where $\partial\Omega$ represents the boundary of the design domain. Inside the design domain (Ω), we can also apply a quasi-static body force, $\bar{\mathbf{b}}(t)$, where $t \in [0, T]$ represents the current time with its maximum denoted as T.

In this work, we focus on the design domain made of isotropic elastoplastic materials under small deformations with combined isotropic and kinematic hardening and a von Mises yield surface. Specifically, we consider a material with an elasticity tensor given by

$$\mathbb{C}^{\mathrm{el}} = \kappa \mathbf{I} \otimes \mathbf{I} + 2\mu \left(\mathbb{I} - \frac{1}{3} \mathbf{I} \otimes \mathbf{I} \right)$$

where κ and μ are the bulk and shear moduli, respectively. For the plasticity-related material properties, we consider materials with the uniaxial yield strength, σ_y, an isotropic hardening modulus, $K = \theta\overline{H}$, and a kinematic hardening modulus, $H = (1-\theta)\overline{H}$, where $\theta \in [0, 1]$ and $\overline{H}$ are two prescribed constants.

Based on the above setups, the flow rules and hardening laws of the J_2-flow plasticity theory (Simo and Hughes, 2006) are given as

$$\begin{cases} \xi = \mathbf{s} - \boldsymbol{\beta}, \quad f(\xi, \alpha) = \|\xi\| - \sqrt{\frac{2}{3}}(\sigma_y + \theta\overline{H}\alpha), \\ \dot{\varepsilon}^p = \gamma \mathbf{n}, \quad \dot{\boldsymbol{\beta}} = \frac{2}{3}\gamma(1-\theta)\overline{H}\mathbf{n}, \quad \dot{\alpha} = \sqrt{\frac{2}{3}}\gamma. \end{cases} \tag{1}$$

Here, the variable ξ is the net stress tensor. The variable $\mathbf{s} = \mathrm{dev}(\boldsymbol{\sigma})$ is the deviatoric part of the stress tensor ($\boldsymbol{\sigma}$), and $\mathrm{dev}(\cdot) = (\cdot) - \mathrm{tr}(\cdot)\mathbf{I}/3$ is the deviatoric operator. The variable $\boldsymbol{\beta}$, subjected to $\mathrm{tr}(\boldsymbol{\beta}) = 0$, is the back stress tensor characterizing the center of the von Mises yield surface. The variable $f(\xi, \alpha)$ is a yield surface indicator with $f = 0$ representing that a material point has entered the plastic state. The operator $\|\cdot\|$ represents the Frobenius norm, and therefore, $\|\xi\| = \sqrt{\xi : \xi}$. The variable α is the cumulative equivalent plastic strain, which is non-decreasing over time. The variable $\dot{\varepsilon}^p$ is the plastic strain rate, and the operator $\dot{(\cdot)}$ represents the time derivative. The variable γ is a consistency parameter, and $\mathbf{n} := \xi/\|\xi\|$. In addition to the above flow rules and hardening laws, the plasticity behavior also adheres to the Kuhn–Tucker conditions expressed as

$$\gamma \geq 0, \quad f(\xi,\alpha) \leq 0, \quad \text{and} \quad \gamma f(\xi,\alpha) = 0. \tag{2}$$

2.2. Return mapping algorithm

Based on (1)–(2) and using a time discretization scheme (backward Euler in this study), obtaining the stress under a strain increment can be achieved by the (radial) return mapping algorithm (Krieg and Krieg, 1977; Simo and Taylor, 1986). We begin by discretizing the continuous time interval ($[0,T]$) into a series of a discrete times, $\{0 = t_0, t_1, \dots, t_n, t_{n+1}, \dots, t_{N^{\text{step}}-1}, t_{N^{\text{step}}} = T\}$, corresponding to N^{step} load steps. Next, given the deviatoric plastic strain tensor ($\mathbf{e}^p_n$), back stress tensor ($\boldsymbol{\beta}_n$), and cumulative equivalent plastic strain (α_n) at load step n as well as the infinitesimal total strain tensor ($\boldsymbol{\varepsilon}_{n+1}$) at load step $n+1$, we rewrite (1) into a time-discretized form as

$$\begin{cases} \mathbf{e}_{n+1} = \boldsymbol{\varepsilon}_{n+1} - \frac{1}{3}\text{tr}(\boldsymbol{\varepsilon}_{n+1})\mathbf{I}, & \mathbf{e}^p_{n+1} = \mathbf{e}^p_n + \Delta\gamma \mathbf{n}_{n+1}, \\ \mathbf{s}_{n+1} = 2\mu(\mathbf{e}_{n+1} - \mathbf{e}^p_{n+1}), & \mathbf{s}^{\texttt{trial}}_{n+1} := 2\mu(\mathbf{e}_{n+1} - \mathbf{e}^p_n), \\ \boldsymbol{\xi}_{n+1} = \mathbf{s}_{n+1} - \boldsymbol{\beta}_{n+1}, & \boldsymbol{\xi}^{\texttt{trial}}_{n+1} := \mathbf{s}^{\texttt{trial}}_{n+1} - \boldsymbol{\beta}_n, \\ \mathbf{n}_{n+1} = \dfrac{\boldsymbol{\xi}_{n+1}}{\|\boldsymbol{\xi}_{n+1}\|}, & \mathbf{n}^{\texttt{trial}}_{n+1} := \dfrac{\boldsymbol{\xi}^{\texttt{trial}}_{n+1}}{\|\boldsymbol{\xi}^{\texttt{trial}}_{n+1}\|}, \\ \boldsymbol{\beta}_{n+1} = \boldsymbol{\beta}_n + \frac{2}{3}\Delta\gamma(1-\theta)\overline{H}\mathbf{n}_{n+1}, & \alpha_{n+1} = \alpha_n + \sqrt{\frac{2}{3}}\Delta\gamma, \\ f_{n+1} = \|\boldsymbol{\xi}_{n+1}\| - \sqrt{\frac{2}{3}}(\sigma_y + \theta\overline{H}\alpha_{n+1}), & f^{\texttt{trial}}_{n+1} := \|\boldsymbol{\xi}^{\texttt{trial}}_{n+1}\| - \sqrt{\frac{2}{3}}(\sigma_y + \theta\overline{H}\alpha_n). \end{cases} \tag{3}$$

Here, we set $\Delta\gamma := \gamma(t_{n+1} - t_n)$ and utilize the relationships of

$$\mathbf{e}_{n+1} := \text{dev}(\boldsymbol{\varepsilon}_{n+1}), \quad \mathbf{e}^p_{n+1} := \text{dev}(\boldsymbol{\varepsilon}^p_{n+1}) = \boldsymbol{\varepsilon}^p_{n+1}, \quad \boldsymbol{\sigma}_{n+1} = \mathbb{C}^{\text{el}} : (\boldsymbol{\varepsilon}_{n+1} - \boldsymbol{\varepsilon}^p_{n+1}), \quad \mathbf{s}_{n+1} = \text{dev}(\boldsymbol{\sigma}_{n+1}).$$

The symbols $(\cdot)_n$ and $(\cdot)_{n+1}$ in (3) represent the state variables at load steps n and $n+1$, respectively. The variable with a superscript of `trial` represents its trial state.

Based on the above equations, we can prove

$$\begin{cases} \|\boldsymbol{\xi}_{n+1}\| + \Delta\gamma\left[2\mu + \frac{2}{3}(1-\theta)\overline{H}\right] = \|\boldsymbol{\xi}^{\texttt{trial}}_{n+1}\| \\ \mathbf{n}_{n+1} = \mathbf{n}^{\texttt{trial}}_{n+1} \end{cases}$$

by noticing $\|\mathbf{n}_{n+1}\| = \|\mathbf{n}^{\texttt{trial}}_{n+1}\| = 1$, which yields

$$f_{n+1} = f^{\texttt{trial}}_{n+1} - \Delta\gamma\left(2\mu + \frac{2\overline{H}}{3}\right).$$

Applying the Kuhn–Tucker conditions in (2) further renders

$$\Delta\gamma = \frac{\langle f^{\texttt{trial}}_{n+1}\rangle}{2\mu + \frac{2\overline{H}}{3}}, \tag{4}$$

where the operator $\langle\cdot\rangle = [(\cdot) + |\cdot|]/2$ takes the positive part of a scalar. Once the parameter $\Delta\gamma$ is computed, we can update the deviatoric plastic strain tensor ($\mathbf{e}^p_{n+1}$), back stress tensor ($\boldsymbol{\beta}_{n+1}$), and cumulative equivalent plastic strain (α_{n+1}) at load step $n+1$. We then repeat this procedure until the last load step (N^{step}).

The above return mapping algorithm is summarized in Algorithm 1. Note that Algorithm 1 also computes the stress tensor in (5) and the consistent tangent modulus in (6), which will be introduced in the next subsection. We also summarize this computational procedure in a flowchart in Fig. 2. Based on the flowchart, the independent state variables are the plastic strain ($\mathbf{e}^p_n$), back stress ($\boldsymbol{\beta}_n$), and cumulative equivalent plastic strain (α_n) at load step n as well as the displacement ($\mathbf{u}_{n+1}$) at load step $n+1$. This information about independent state variables will be exploited in sensitivity analysis in Appendix A.

2.3. Solution scheme of finite element analysis

The J_2-flow plasticity theory in Section 2.1 and the associated return mapping algorithm in Section 2.2 predict the elastoplastic response of a single material point within the design domain (Ω). To extend these predictions to the structural responses of the entire design domain, we employ a solution scheme based on the well-established FEA (Simo and Hughes, 2006) as introduced below.

Algorithm 1: Return mapping algorithm with a backward Euler integration scheme

Inputs: deviatoric plastic strain tensor, $\mathbf{e}_n^p$; back stress tensor, $\boldsymbol{\beta}_n$; cumulative equivalent plastic strain, α_n; total strain tensor, $\boldsymbol{\varepsilon}_{n+1} = \boldsymbol{\varepsilon}(\mathbf{u}_{n+1})$;
Prediction stage:
  Compute the deviatoric strain tensor, $\mathbf{e}_{n+1}$, based on $\boldsymbol{\varepsilon}_{n+1}$;
  Compute the trial deviatoric stress tensor, $\mathbf{s}_{n+1}^{\mathtt{trial}}$, based on $\mathbf{e}_{n+1}$ and $\mathbf{e}_n^p$;
  Compute the trial net stress tensor, $\boldsymbol{\xi}_{n+1}^{\mathtt{trial}}$, based on $\mathbf{s}_{n+1}^{\mathtt{trial}}$ and $\boldsymbol{\beta}_n$;
  Compute the trial yield surface indicator, $f_{n+1}^{\mathtt{trial}}$, based on $\boldsymbol{\xi}_{n+1}^{\mathtt{trial}}$ and α_n;
  Compute the parameter $\Delta\gamma$ in (4) based on $f_{n+1}^{\mathtt{trial}}$;
Correction stage:
  Compute the unit tensor, $\mathbf{n}_{n+1} = \mathbf{n}_{n+1}^{\mathtt{trial}}$, based on $\boldsymbol{\xi}_{n+1}^{\mathtt{trial}}$;
  Update the state variables, $\mathbf{e}_{n+1}^p$, $\boldsymbol{\beta}_{n+1}$, and α_{n+1}, based on $\mathbf{e}_n^p$, $\boldsymbol{\beta}_n$, α_n, $\Delta\gamma$, and $\mathbf{n}_{n+1}$;
  Compute the stress tensor, $\boldsymbol{\sigma}_{n+1}$ in (5), based on $\boldsymbol{\varepsilon}_{n+1}$, $\mathbf{s}_{n+1}^{\mathtt{trial}}$, $\Delta\gamma$, and $\mathbf{n}_{n+1}$;
  Compute the consistent tangent modulus, $\widehat{\mathbb{C}}_{n+1}^{\mathtt{tang}}$ in (6), based on $\Delta\gamma$, $\boldsymbol{\xi}_{n+1}^{\mathtt{trial}}$, $f_{n+1}^{\mathtt{trial}}$, and $\mathbf{n}_{n+1}$;

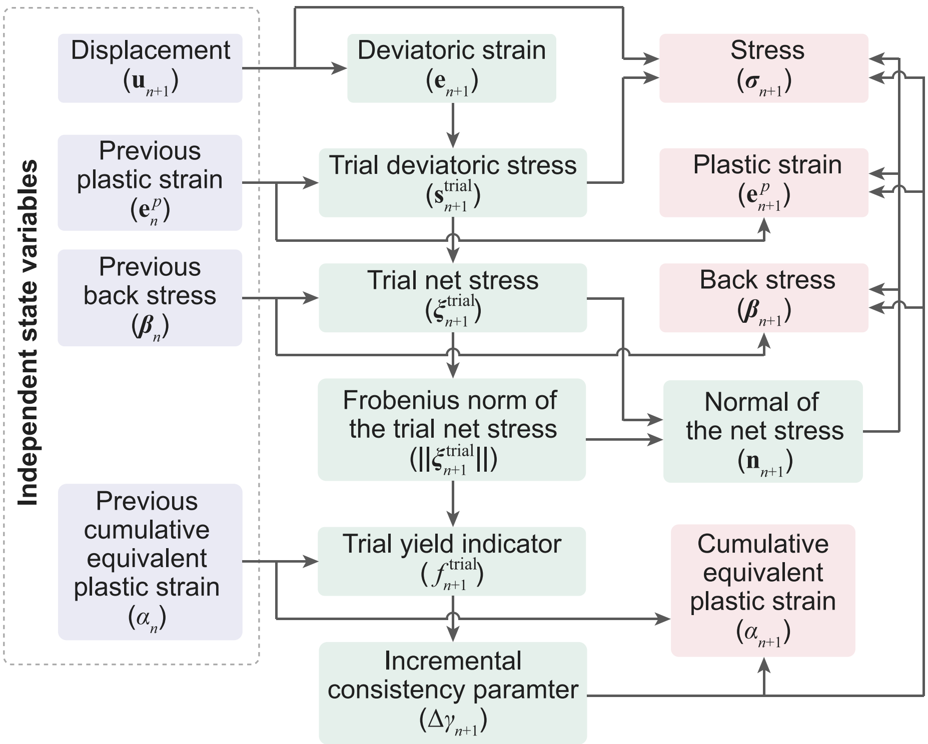

Fig. 2. Identifying the independent state variables in the local hardening laws and flow rules in (3).

We begin by computing the stress tensor at load step $n+1$ as

$$\boldsymbol{\sigma}_{n+1} = \kappa \operatorname{tr}(\boldsymbol{\varepsilon}_{n+1})\mathbf{I} + \mathbf{s}_{n+1}^{\mathtt{trial}} - 2\mu\Delta\gamma\mathbf{n}_{n+1} \tag{5}$$

and the consistent tangent modulus ($\mathbb{C}_{n+1}^{\mathtt{tang}}$) as

$$\mathbb{C}_{n+1}^{\mathtt{tang}} = \frac{d\boldsymbol{\sigma}_{n+1}}{d\boldsymbol{\varepsilon}_{n+1}} = \begin{cases} \mathbb{C}^{\mathtt{el}} \equiv \kappa\mathbf{I}\otimes\mathbf{I} + 2\mu\left(\mathbb{I} - \frac{1}{3}\mathbf{I}\otimes\mathbf{I}\right), & f_{n+1}^{\mathtt{trial}} \leq 0 \\ \mathbb{C}_{n+1}^{\mathtt{ep}} := \kappa\mathbf{I}\otimes\mathbf{I} + 2\mu\eta_{n+1}\left(\mathbb{I} - \frac{1}{3}\mathbf{I}\otimes\mathbf{I}\right) - 2\mu\overline{\eta}_{n+1}\mathbf{n}_{n+1}\otimes\mathbf{n}_{n+1}, & f_{n+1}^{\mathtt{trial}} > 0 \end{cases}$$

where the parameters η_{n+1} and $\overline{\eta}_{n+1}$ are given as

$$\eta_{n+1} = 1 - \Delta\gamma \frac{2\mu}{\|\xi^{\mathtt{trial}}_{n+1}\|} \quad \text{and} \quad \bar{\eta}_{n+1} = \frac{1}{1+\dfrac{\overline{H}}{3\mu}} - (1-\eta_{n+1}),$$

respectively, and the variable $\mathbb{C}^{\mathrm{ep}}_{n+1}$ represents the elastoplastic modulus at load step $n+1$. For convenience, we rescale the last term in $\mathbb{C}^{\mathrm{ep}}_{n+1}$ with a coefficient $\langle f^{\mathtt{trial}}_{n+1}\rangle / f^{\mathtt{trial}}_{n+1}$ and reformulate the consistent tangent modulus in a more concise way as

$$\widehat{\mathbb{C}}^{\mathtt{tang}}_{n+1} = \kappa \mathbf{I}\otimes\mathbf{I} + 2\mu\eta_{n+1}\left(\mathbb{I} - \frac{1}{3}\mathbf{I}\otimes\mathbf{I}\right) - 2\mu\bar{\eta}_{n+1}\frac{\langle f^{\mathtt{trial}}_{n+1}\rangle}{f^{\mathtt{trial}}_{n+1}}\mathbf{n}_{n+1}\otimes\mathbf{n}_{n+1}. \tag{6}$$

Based on the consistent tangent modulus in (6), we can employ the Newton–Raphson method to formulate a time-discretized weak form for solving the incremental displacement, $\mathrm{d}\mathbf{u}^{k+1}_{n+1} = \mathbf{u}^{k+1}_{n+1} - \mathbf{u}^{k}_{n+1}$, at iteration $k+1$ and load step $n+1$. The weak form is defined as finding $\mathrm{d}\mathbf{u}^{k+1}_{n+1} \in \mathcal{U}$ such that for all $\mathbf{v}\in\mathcal{V}$

$$\int_{\Omega} \boldsymbol{\sigma}^{\mathtt{tang}}(\boldsymbol{\varepsilon}(\mathrm{d}\mathbf{u}^{k+1}_{n+1}); \boldsymbol{\varepsilon}(\mathbf{u}^{k}_{n+1})) : \boldsymbol{\varepsilon}(\mathbf{v})\mathrm{d}\mathbf{X} = \int_{\Omega} \bar{\mathbf{b}}_{n+1}\cdot\mathbf{v}\mathrm{d}\mathbf{X} + \int_{\partial\Omega_{\mathcal{N}}} \bar{\mathbf{t}}_{n+1}\cdot\mathbf{v}\mathrm{d}\mathbf{X} - \int_{\Omega}\boldsymbol{\sigma}(\boldsymbol{\varepsilon}(\mathbf{u}^{k}_{n+1})) : \boldsymbol{\varepsilon}(\mathbf{v})\mathrm{d}\mathbf{X} \tag{7}$$

where $\mathbf{v}$ is the test displacement field. The function spaces $\mathcal{U}$ and $\mathcal{V}$ are expressed as

$$\begin{cases} \mathcal{U} = \{\mathrm{d}\mathbf{u} \in H^1(\Omega\cup\partial\Omega;\mathbb{R}^3) : \mathrm{d}\mathbf{u} = \bar{\mathbf{u}}_{n+1} - \mathbf{u}^{k}_{n+1} \text{ on } \partial\Omega_{D}\}, \\ \mathcal{V} = \{\mathbf{v} \in H^1(\Omega\cup\partial\Omega;\mathbb{R}^3) : \mathbf{v} = \mathbf{0} \text{ on } \partial\Omega_{D}\}. \end{cases}$$

The variable $\boldsymbol{\sigma}^{\mathtt{tang}}$ in (7) is given as

$$\begin{aligned} \boldsymbol{\sigma}^{\mathtt{tang}}(\boldsymbol{\varepsilon}(\mathrm{d}\mathbf{u}^{k+1}_{n+1}); \boldsymbol{\varepsilon}(\mathbf{u}^{k}_{n+1})) &= \widehat{\mathbb{C}}^{\mathtt{tang}}(\boldsymbol{\varepsilon}(\mathbf{u}^{k}_{n+1}); \mathbf{e}^p_n, \boldsymbol{\beta}_n, \alpha_n) : \boldsymbol{\varepsilon}(\mathrm{d}\mathbf{u}^{k+1}_{n+1}) \\ &= \kappa\,\mathrm{tr}(\boldsymbol{\varepsilon}(\mathrm{d}\mathbf{u}^{k+1}_{n+1}))\mathbf{I} + 2\mu\eta(\boldsymbol{\varepsilon}(\mathbf{u}^{k}_{n+1}))\mathrm{dev}(\boldsymbol{\varepsilon}(\mathrm{d}\mathbf{u}^{k+1}_{n+1})) \\ &\quad - 2\mu\bar{\eta}(\boldsymbol{\varepsilon}(\mathbf{u}^{k}_{n+1}))\frac{\langle f^{\mathtt{trial}}\rangle}{f^{\mathtt{trial}}}(\boldsymbol{\varepsilon}(\mathbf{u}^{k}_{n+1}))\mathbf{n}(\boldsymbol{\varepsilon}(\mathbf{u}^{k}_{n+1})) : \boldsymbol{\varepsilon}(\mathrm{d}\mathbf{u}^{k+1}_{n+1})\mathbf{n}(\boldsymbol{\varepsilon}(\mathbf{u}^{k}_{n+1})). \end{aligned}$$

Finally, the overall solution procedure of FEA is summarized in Algorithm 2.

Algorithm 2: Solution procedure of FEA for small-deformation elastoplasticity

Inputs: the number of load steps, $N^{\mathtt{step}}$; the number of allowable Newton iterations, $N^{\mathtt{iter}}$; the tolerance of the displacement increment, $\varepsilon^{\mathtt{tol}}$;
Initialization: deviatoric plastic strain tensor, $\mathbf{e}^p_0 \leftarrow \mathbf{0}$; back stress tensor, $\boldsymbol{\beta}_0 \leftarrow \mathbf{0}$; cumulative equivalent plastic strain, $\alpha_0 \leftarrow 0$; displacement field, $\mathbf{u}_0 \leftarrow \mathbf{0}$; stress tensor, $\boldsymbol{\sigma}_0 \leftarrow \mathbf{0}$; consistent tangent modulus, $\widehat{\mathbb{C}}^{\mathtt{tang}}_0 \leftarrow \mathbb{C}^{\mathtt{el}}$; load step counter, $n \leftarrow 0$;
while $n < N^{step}$ **do**
    Set the initial displacement field, $\mathbf{u}^0_{n+1} \leftarrow \mathbf{u}_n$, stress tensor, $\boldsymbol{\sigma}^0_{n+1} \leftarrow \boldsymbol{\sigma}_n$, and the consistent tangent modulus, $\widehat{\mathbb{C}}^{\mathtt{tang},0}_{n+1} \leftarrow \widehat{\mathbb{C}}^{\mathtt{tang}}_{n}$;
    Apply the boundary conditions, $\bar{\mathbf{b}}_{n+1}$, $\bar{\mathbf{t}}_{n+1}$, and $\bar{\mathbf{u}}_{n+1}$;
    Reset the iteration counter, $k \leftarrow 0$;
    while $k < N^{iter}$ **do**
        Solve (7) for the displacement increment at the current iteration, $\mathrm{d}\mathbf{u}^{k+1}_{n+1}$, based on the stress tensor, $\boldsymbol{\sigma}^k_{n+1}$, and the consistent tangent modulus, $\widehat{\mathbb{C}}^{\mathtt{tang},k}_{n+1}$;
        Update the displacement field as $\mathbf{u}^{k+1}_{n+1} \leftarrow \mathbf{u}^{k}_{n+1} + \mathrm{d}\mathbf{u}^{k+1}_{n+1}$;
        Compute the stress tensor, $\boldsymbol{\sigma}^{k+1}_{n+1}$, and the consistent tangent modulus, $\widehat{\mathbb{C}}^{\mathtt{tang},k+1}_{n+1}$, by substituting $\boldsymbol{\varepsilon}(\mathbf{u}^{k+1}_{n+1})$, $\mathbf{e}^p_n$, $\boldsymbol{\beta}_n$, and α_n into the return mapping scheme in Algorithm 1.
        Compute the 2-norm of the current displacement increment as $r_{k+1} = \|\mathrm{d}\mathbf{u}^{k+1}_{n+1}\|_2$;
        if $r_{k+1}/r_1 \leq \varepsilon^{tol}$ **then**
            Break the while-loop for the Newton iterations;
        Update the iteration counter, $k \leftarrow k+1$;
    end
    Record the converged displacement field, $\mathbf{u}_{n+1} \leftarrow \mathbf{u}^{k+1}_{n+1}$, stress tensor, $\boldsymbol{\sigma}_{n+1} \leftarrow \boldsymbol{\sigma}^{k+1}_{n+1}$, and consistent tangent modulus, $\widehat{\mathbb{C}}^{\mathtt{tang}}_{n+1} \leftarrow \widehat{\mathbb{C}}^{\mathtt{tang},k+1}_{n+1}$;
    Compute the converged history variables, $\mathbf{e}^p_{n+1}$, $\boldsymbol{\beta}_{n+1}$, and α_{n+1}, by substituting $\boldsymbol{\varepsilon}(\mathbf{u}_{n+1})$, $\mathbf{e}^p_n$, $\boldsymbol{\beta}_n$, and α_n into the return mapping scheme in Algorithm 1 ;
    Update the load step counter, $n \leftarrow n+1$;
end

3. Multimaterial elastoplastic topology optimization

Based on the fundamentals of elastoplasticity in Section 2, we introduce a multimaterial and multiobjective topology optimization framework to optimize a wide range of structural elastoplastic responses. The framework consists of design space parameterization, material property interpolation, and topology optimization formulation, which are detailed below.

3.1. Design space parameterization

To optimize elastoplastic structures, we need to identify the design variables that parameterize the material presence and phases. We define a dimensionless scalar density variable, $\rho(\mathbf{X}) \in [0,1]$, to describe the presence of the material and material variables, $\xi_1(\mathbf{X}),\ \xi_2(\mathbf{X}),\ \ldots,\ \xi_{N^{\mathtt{mat}}-1}(\mathbf{X}) \in [0,1]$, to represent material phases. Here, $\mathbf{X} \in \Omega$ is the position vector of a material point in the design domain (Ω), and $N^{\mathtt{mat}}$ is the number of available material phases. To alleviate mesh dependency, eliminate the checkerboard pattern, promote a discrete design, and impose an equality constraint for material variables, we convert these design variables (ρ and ξ_1–$\xi_{N^{\mathtt{mat}}-1}$) to physical variables ($\overline{\rho}$ and $\overline{\xi}_1$–$\overline{\xi}_{N^{\mathtt{mat}}}$) through a linear filter (Bourdin, 2001), Heaviside projection (Bendsoe and Sigmund, 2003), and a modified version of HSP (Zhou et al., 2018). The details are provided in Appendix B.

The resulting physical variables have the following meanings. The physical density variable $\overline{\rho}(\mathbf{X}) = 1$ represents a solid material point, while $\overline{\rho}(\mathbf{X}) = 0$ represents a void. The physical material variables, $\overline{\xi}_1(\mathbf{X}),\ \overline{\xi}_2(\mathbf{X}),\ \ldots,\ \overline{\xi}_{N^{\mathtt{mat}}}(\mathbf{X}) \in [0,1]$, represent the volume fractions of material phases $1,2,\ldots,N^{\mathtt{mat}}$ at the material point $\mathbf{X}$, respectively. Based on this design space parameterization, we can conveniently characterize material presence and phases through the physical density ($\overline{\rho}$) and material ($\overline{\xi}_1$–$\overline{\xi}_{N^{\mathtt{mat}}}$) variables, respectively.

3.2. Material property interpolation

After parameterizing the design space with physical variables ($\overline{\rho}$ and $\overline{\xi}_1$–$\overline{\xi}_{N^{\mathtt{mat}}}$), we need to interpolate the material properties for various values of these variables. While existing studies interpolate the properties for density or material variables alone, we simultaneously account for both factors by adapting a multimaterial interpolation rule for hyperelasticity (Li et al., 2023) to the elastoplasticity considered here. The interpolation rules read as

$$\begin{cases} \chi(\overline{\rho},\overline{\xi}_1,\overline{\xi}_2,\ldots,\overline{\xi}_{N^{\mathtt{mat}}}) = \left[\varepsilon_\rho + (1-\varepsilon_\rho)\overline{\rho}^{p_\rho^\chi}\right] \displaystyle\sum_{n=1}^{N^{\mathtt{mat}}} \overline{\xi}_n^{p_\xi} \chi_0^{[n]} \quad \text{for} \quad \chi \in \{E, K, H, \sigma_y\}, \\ \nu(\overline{\xi}_1,\overline{\xi}_2,\ldots,\overline{\xi}_{N^{\mathtt{mat}}}) = \displaystyle\sum_{n=1}^{N^{\mathtt{mat}}} \overline{\xi}_n^{p_\xi} \nu_0^{[n]}. \end{cases}$$

Here, the variable χ stands for a generic interpolated material property. The variables E and ν are the interpolated Young's modulus and Poisson's ratio, respectively. The variables K and H are the interpolated isotropic and kinematic hardening moduli, respectively. The variable σ_y is the interpolated uniaxial yield strength. The subscript 0 represents the material property of the corresponding single-phase solid material, and the superscript $[n]$ represents the nth material phase. Additionally, the parameter $p_\rho^\chi \in \{p_\rho^E, p_\rho^K, p_\rho^H, p_\rho^{\sigma_y}\}$ penalizes the intermediate physical density variable, $\overline{\rho} \in (0,1)$, and we adopt $p_\rho^E = p_\rho^K = p_\rho^H = 3$ and $p_\rho^{\sigma_y} \in [1.5, 2.5]$ based on q–p relaxation (Bruggi, 2008). The parameter $p_\xi \in [1,3]$ penalizes the intermediate physical material variables, $\overline{\xi}_1$–$\overline{\xi}_{N^{\mathtt{mat}}} \in (0,1)$. The parameter $\varepsilon_\rho = 10^{-6}$ prevents the singularity of the stiffness matrix in FEA.

3.3. Multiobjective topology optimization formulation

Based on design space parameterization and material property interpolation, we now introduce the multimaterial and multiobjective topology optimization formulation as

$$\begin{cases} \underset{\rho,\ \xi_1,\ \ldots,\ \xi_{N^{\mathtt{mat}}-1}}{\text{minimize}} \quad : \quad J(\overline{\rho},\overline{\xi}_1,\ldots,\overline{\xi}_{N^{\mathtt{mat}}};\mathbf{u}_1,\ldots,\mathbf{u}_{N^{\mathtt{step}}};\mathbf{e}_1^p,\ldots,\mathbf{e}_{N^{\mathtt{step}}}^p;\boldsymbol{\beta}_1,\ldots,\boldsymbol{\beta}_{N^{\mathtt{step}}};\alpha_1,\ldots,\alpha_{N^{\mathtt{step}}}); \\ \text{subject to} : \quad \begin{cases} g_1(\overline{\rho}) = \dfrac{1}{|\Omega|}\displaystyle\int_\Omega \overline{\rho}\,\mathrm{d}\mathbf{X} - \overline{V} \le 0; \\ g_{i+1}(\overline{\rho},\overline{\xi}_i) = \dfrac{1}{|\Omega|}\displaystyle\int_\Omega \overline{\rho}\,\overline{\xi}_i\,\mathrm{d}\mathbf{X} - \overline{V}_i \le 0 \quad \text{for} \quad i = 1,2,\ldots,N^{\mathtt{mat}}; \\ 0 \le \rho \le 1; \\ 0 \le \xi_i \le 1 \quad \text{for} \quad i = 1,2,\ldots,N^{\mathtt{mat}}-1; \end{cases} \\ \quad\text{with:} \quad \text{local hardening laws and flow rules in (3) and global equilibrium equation in (7).} \end{cases} \tag{8}$$

Here, J is a general objective function to be minimized, whose mathematical form will be introduced later. The variable g_1 is the overall material constraint associated with the total allowable volume fraction, $\overline{V} \in (0,1]$. The variables g_{i+1} for $i = 1,2,\ldots,N^{\mathtt{mat}}$ are the individual material constraints for materials $1,2,\ldots,N^{\mathtt{mat}}$ with the individual allowable volume fractions, $\overline{V}_1,\overline{V}_2,\ldots,\overline{V}_{N^{\mathtt{mat}}} \in (0,1]$, respectively.

In this work, we aim to design structures with optimized elastoplastic responses. To achieve this goal, we adopt a multiobjective function defined as

$$J = -(w_{\mathtt{elas,I}}W_{\mathtt{elas,I}} - w_{\mathtt{plas,I}}W_{\mathtt{plas,I}}) - (w_{\mathtt{elas,II}}W_{\mathtt{elas,II}} + w_{\mathtt{plas,II}}W_{\mathtt{plas,II}}). \tag{9}$$

Subscripts I and II refer to the two stages of the loading histories shown in Fig. 3, which are separated by a chosen critical displacement, $u_{\mathtt{crit}}$, or a chosen critical load step, $M \in \{0,1,2,\ldots,N^{\mathtt{step}}\}$. The parameters $w_{\mathtt{elas,I}}$, $w_{\mathtt{plas,I}}$, $w_{\mathtt{elas,II}}$, and $w_{\mathtt{plas,II}} \in [0,1]$ are weighting factors subjected to $w_{\mathtt{elas,I}} + w_{\mathtt{plas,I}} + w_{\mathtt{elas,II}} + w_{\mathtt{plas,II}} = 1$. The variables $W_{\mathtt{elas,I}}$ and $W_{\mathtt{plas,I}}$ are the elastic and

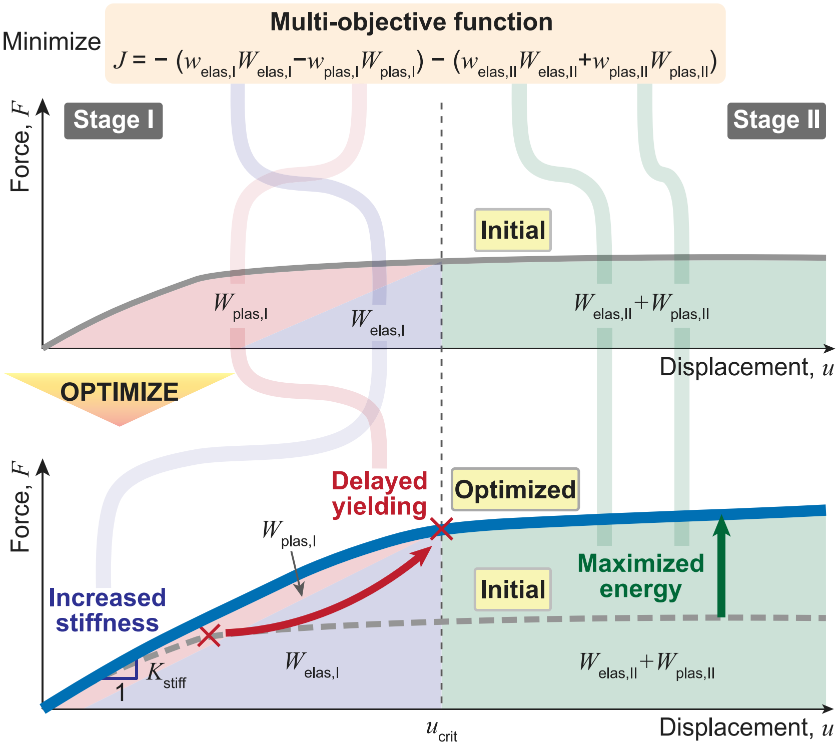

Fig. 3. Illustration of the multiobjective function in (9). The variable u_{crit} is the critical displacement corresponding to the chosen load step, M.

plastic energies in stage I, respectively, and $W_{\text{elas,II}}$ and $W_{\text{plas,II}}$ are the counterparts in stage II. These energies can be expressed as

$$\begin{cases} W_{\text{elas,I}} = \dfrac{1}{2}\displaystyle\sum_{n=1}^{M}\int_{\Omega}(\boldsymbol{\sigma}_n + \boldsymbol{\sigma}_{n-1}) : [(\boldsymbol{\varepsilon}_n - \boldsymbol{\varepsilon}_n^p) - (\boldsymbol{\varepsilon}_{n-1} - \boldsymbol{\varepsilon}_{n-1}^p)]\mathrm{d}\mathbf{X}, \\ W_{\text{plas,I}} = \dfrac{1}{2}\displaystyle\sum_{n=1}^{M}\int_{\Omega}(\boldsymbol{\sigma}_n + \boldsymbol{\sigma}_{n-1}) : (\boldsymbol{\varepsilon}_n^p - \boldsymbol{\varepsilon}_{n-1}^p)\mathrm{d}\mathbf{X}, \\ W_{\text{elas,II}} = \dfrac{1}{2}\displaystyle\sum_{n=M+1}^{N^{\text{step}}}\int_{\Omega}(\boldsymbol{\sigma}_n + \boldsymbol{\sigma}_{n-1}) : [(\boldsymbol{\varepsilon}_n - \boldsymbol{\varepsilon}_n^p) - (\boldsymbol{\varepsilon}_{n-1} - \boldsymbol{\varepsilon}_{n-1}^p)]\mathrm{d}\mathbf{X}, \\ W_{\text{plas,II}} = \dfrac{1}{2}\displaystyle\sum_{n=M+1}^{N^{\text{step}}}\int_{\Omega}(\boldsymbol{\sigma}_n + \boldsymbol{\sigma}_{n-1}) : (\boldsymbol{\varepsilon}_n^p - \boldsymbol{\varepsilon}_{n-1}^p)\mathrm{d}\mathbf{X}. \end{cases}$$

By minimizing the multiobjective function in (9), we aim to achieve several goals simultaneously (Fig. 3). First, we maximize $W_{\text{elas,I}}$ to increase the initial structural stiffness, which is positively correlated with strain energy under displacement loading. Second, we minimize $w_{\text{plas,I}}$ to reduce plastic energy, thereby delaying structural yielding up to the critical displacement (u_{crit}; corresponding to the chosen load step, M). Furthermore, once the structure yields, we maximize elastic energy absorption through $W_{\text{elas,II}}$ and plastic energy dissipation through $W_{\text{plas,II}}$. By optimizing this multiobjective function, we can effectively design elastoplastic structures for various applications, such as dampers and yield-resistant structures as demonstrated in Section 4.

4. Representative case studies

In this section, we present three representative case studies to demonstrate free-form and multimaterial metallic structures with diverse optimized elastoplastic responses and reveal their underlying mechanical mechanisms. First, we maximize the plastic energy dissipation of metallic yield dampers. We illustrate the effectiveness of the proposed formulation (8) in improving plastic energy compared to a reference design with maximized stiffness. We also show that the composite structure outperforms single-material ones, an aspect often overlooked in related studies. Additionally, we investigate the optimized dampers under increasing applied displacements, revealing a stiff-to-strong transition that maximizes energy dissipation.

Next, we examine yield-resistant elastoplastic structures that simultaneously maximize initial stiffness and total energy while delaying yielding. These structures exhibit tunable trade-offs among stiffness, strength, and toughness in various combinations of

Table 1
Properties of candidate materials used in case studies.

Materials	Young's moduli (E in GPa)	Poisson's ratios (ν)	Isotropic hardening moduli (K in MPa)	Kinematic hardening moduli (H in MPa)	Yield strengths (σ_y in MPa)
Titanium (Ti-6Al-4V)	111	0.34	1190	1190	853
Stainless steel (AISI 316L)	195	0.27	670	670	226
Nickel–chromium (Inconel 718)	198	0.30	570	570	770
Bronze (CuSn10)	80	0.35	480	480	145

weighting factors and critical displacement in (9). Importantly, we reveal a parallel arrangement of distinct alloys to decouple structural yielding from material yielding and prevent catastrophic structural failure. We also uncover a mechanism for delaying yielding by forming self-equilibrating structures that alter the load paths.

Finally, we inspect two optimized multi-alloy structures in three dimensions (3D). These optimized structures demonstrate an enhanced total energy through more distributed plastic regions compared to a reference design. Moreover, they delay the yielding by placing stronger materials around areas subjected to external loading.

The material properties used in these case studies are provided in Table 1. Here, we recall that the isotropic and kinematic hardening moduli are defined as $K = \theta\overline{H}$ and $H = (1-\theta)\overline{H}$, respectively, and we adopt $\theta = 0.5$ ($K = H$) for all candidate materials. These candidate materials cover a wide range of elastic and plastic properties. More importantly, each pair of these four materials can be jointed via additive manufacturing as reported in Wei et al. (2020, 2022), and we assume perfect bonding in the current work for simplicity.

To perform the proposed topology optimization framework in these case studies, we extend the open-source FEniTop software (Jia et al., 2024d) (FEniCSx (Baratta et al., 2023)-based topology optimization) to account for the nonlinear and history-dependent elastoplastic responses. During topology optimization, we solve the nonlinear FEA with the Newton–Raphson method (see Algorithm 2), which decomposes the FEA problem into a series of linear equations in (7). To maintain solution accuracy, we solve the decomposed linear equations with a direct solver through lower–upper (LU) factorization. To update the design variables (ρ and ξ_1–$\xi_{N^{\mathtt{mat}}-1}$), we leverage the reversed adjoint method and automatic differentiation (see Appendix A) to compute the sensitivities, which are then fed into a gradient-based optimizer, the Method of Moving Asymptotes (MMA) (Svanberg, 1987). To accelerate the topology optimization process, we utilize parallel computing with 16 threads for two-dimensional (2D) cases and 32 threads for 3D cases through the message passing interface (MPI) (Dalcín et al., 2005). Detailed analyses of case studies are provided below.

4.1. Metallic dampers with maximized energy dissipation

In this subsection, we design metallic yield dampers with maximized energy dissipation, which can be potentially used for structural vibration mitigation (Zhang et al., 2018; Jia et al., 2022). This case study examines the effectiveness of the proposed framework in maximizing the plastic energy of structures. It also demonstrates the advantage of using multiple materials in achieving higher energy dissipation. Additionally, we compare the optimized elastoplastic designs under a wide range of applied displacements and reveal the transition from stiffness-dominance to strength-dominance in achieving maximized energy dissipation.

4.1.1. Single-material versus multimaterial dampers

We begin by showing the effectiveness of the proposed framework in enhancing plastic energy dissipation and highlighting the performance gains achieved by using multiple alloys. As shown in Fig. 4(a), the design domain is a rectangle with a fixed bottom, subjected to simple shear loading with an amplitude of $u = 3.25$ mm. Our goal is to optimally place the materials — among titanium, steel, and void (see material properties in Table 1 and stress–strain curves in Fig. 4(b)) — to maximize plastic energy dissipation (Fig. 4(c)).

To achieve this optimization objective, we adopt the following FEA and topology optimization parameters. The design domain is discretized with a structured mesh containing 60,000 first-order quadrilateral elements. The maximum number of optimization iterations is set to 400. The weighting factors in the objective function in (9) are $w_{\mathtt{elas,I}} = w_{\mathtt{plas,I}} = w_{\mathtt{elas,II}} = 0$ and $w_{\mathtt{plas,II}} = 1$, and the critical displacement is $u_{\mathtt{crit}} = 0$ (corresponding to $M = 0$). The allowable total material volume fraction is $\overline{V} = 0.5$. The filter radii for the density and material variables are $R_\rho = R_\xi = 6$ mm. The Heaviside sharpness parameter for both density and material variables starts at $\beta = 1$ and is doubled every 40 optimization iterations, beginning from iteration 41 until $\beta = 128$. The penalty parameters for the density variable are $p_\rho^E = p_\rho^K = p_\rho^H = 3$ and $p_\rho^{\sigma_y} = 1.5$. The penalty parameter for the material variable starts at $p_\xi = 1$ and is increased by 0.5 every 80 optimization iterations, starting from iteration 41 until $p_\xi = 3$. The move limit in the MMA optimizer is $m = 0.05$. During topology optimization, we use 20 load steps in FEA with the plane strain assumption for all elastoplastic designs and one load step for the stiffness-maximization design (used as a reference). After topology optimization, we employ a fixed displacement interval, $\Delta u = u_{n+1} - u_n \approx 0.1$ mm, for the quasi-static loading to evaluate the elastoplastic responses of all designs.

Based on the above setups, we obtain the optimized dampers and their elastoplastic responses in Fig. 4(d). Here, we include a classical stiffness-maximization design (Dsg. 1) as a reference, which intuitively offers certain energy dissipation. Additionally, we compare three elastoplastic designs generated by the proposed approach — the design using only steel (Dsg. 2), the design using only titanium (Dsg. 3), and the multimaterial design (Dsg. 4) — all optimized for maximum plastic energy dissipation. For all the optimized designs, we examine their optimized material distribution, elastic/plastic regions, and normalized plastic energy density. The elastic/plastic regions are characterized by a state indicator defined as

$$\mathcal{I}(\mathbf{X}) = \begin{cases} \text{Elastic}, & \alpha(\mathbf{X}) < \overline{\alpha} \\ \text{Plastic}, & \alpha(\mathbf{X}) \geq \overline{\alpha} \end{cases}$$

where $\overline{\alpha} = 10^{-4}$ is a prescribed threshold of the cumulative equivalent plastic strain ($\alpha(\mathbf{X})$). The normalized plastic energy density, which describes the unit plastic energy dissipation, can be computed as $\Pi_{\texttt{plas}}(\mathbf{X})/\max(\Pi_{\texttt{plas}}(\mathbf{X}))$. Here, the variable $\Pi_{\texttt{plas}}$ is the plastic energy density defined as

$$\Pi_{\texttt{plas}}(\mathbf{X}) = \frac{1}{2}\sum_{n=1}^{N^{\texttt{step}}} (\boldsymbol{\sigma}_n + \boldsymbol{\sigma}_{n-1}) : (\boldsymbol{\varepsilon}_n^p - \boldsymbol{\varepsilon}_{n-1}^p).$$

According to Fig. 4(d), all three elastoplastic dampers (Dsgs. 2–4) exhibit notable enhancements in energy dissipation (ranging from 6.7% to 14.3%) compared to the stiffness-maximization design (Dsg. 1), demonstrating the effectiveness of the proposed topology optimization formulation in (8). Moreover, among the elastoplastic dampers, the multimaterial design (Dsg. 4) shows the greatest increase in energy dissipation (14.3%) compared to the single-material designs — 6.7% for steel (Dsg. 2) and 7.7% for titanium (Dsg. 3). This comparison reveals the performance gain achieved by simultaneously using multiple alloys.

Upon closer examination of the elastic/plastic regions and normalized plastic energy density in Fig. 4(d), we observe dissimilar behaviors among the designs. Compared to the stiffness-maximization design (Dsg. 1), the steel damper (Dsg. 2) causes nearly all regions to enter the plastic stage by slightly altering the geometries and introducing multiple holes. Conversely, the titanium damper (Dsg. 3) confines plasticity and energy dissipation to the relatively slender regions of the structure. This optimized material distribution is obtained because titanium has a higher yield strength (Fig. 4(b)), and it necessitates the slender regions to concentrate stress and thus promotes yielding and energy dissipation. The multimaterial damper (Dsg. 4) features an organic distribution of titanium and steel materials. In this design, the titanium material does not yield due to its higher strength; however, it can transmit higher stress to the steel materials, causing the steel parts to dissipate more energy.

The performance comparisons of the designs are further investigated in Fig. 4(e). The stiffness-maximization (Dsg. 1) and steel elastoplastic (Dsg. 2) designs have the highest stiffness but the lowest peak forces, while the titanium design (Dsg. 3) exhibits the lowest stiffness but the highest peak force, as reflected in the material properties in Fig. 4(b). The optimized multimaterial plastic design (Dsg. 4) is neither the stiffest nor the strongest (in terms of the highest peak force) but the most energy-dissipative due to the optimized and synergistic use of the two materials. These comparisons demonstrate the effectiveness of the proposed framework in optimizing plastic energy dissipation, which can be further improved by using multiple materials.

4.1.2. Stiff-to-strong transition under increasing applied displacements

We now investigate the influence of applied displacement (u) on the optimized dampers. As shown in Fig. 5, we consider the optimized designs under five different applied displacements: $u \in \{2.00, 2.50, 3.25, 3.50, 4.00\}$ mm. Fig. 5(a)–(c) display the material distribution, elastic/plastic regions, and normalized plastic energy density of the optimized designs under five different applied displacements, respectively.

The observations are as follows. First, all five optimized dampers feature inclined structural members that align with the shear load path. This alignment allows the designs to maintain sufficient initial stiffness and directly contributes to maximized plastic energy dissipation (see Fig. 4(c)).

Second, the optimized dampers prefer the stiffer steel material for lower applied displacements (Dsgs. 1 and 2) and the stronger (but less stiff) titanium material for higher applied displacements (Dsgs. 4 and 5). This transition in material preference reveals that plastic energy dissipation is governed by stiffness at smaller displacements and by peak force at larger displacements. Specifically, smaller applied displacements require the structure to yield early to dissipate more energy, which is achieved by increasing stiffness and stress (under displacement loading). By contrast, under higher applied displacements, the plastic energy is proportional to $F_{\text{peak}} \cdot u$ (see Fig. 4(c)), where F_{peak} represents the peak force. The optimized designs, therefore, favor higher peak forces enabled by titanium for its higher strength (σ_y) and larger hardening moduli (K and H).

Furthermore, by comparing the material distribution in Fig. 5(a) with the elastic/plastic regions in Fig. 5(b), we observe that titanium material rarely yields and does not directly contribute to energy dissipation. However, titanium is still indispensable and advantageous, especially for designs under higher applied displacements, because it increases the stress magnitude in steel and promotes overall energy dissipation.

Finally, Figs. 5(d) and (e) present the force–displacement and plastic energy–displacement curves of the optimized designs, respectively. As previously mentioned, the optimized designs exhibit reduced stiffness and increasing peak forces as the applied displacement increases. Additionally, the optimized designs show delayed yielding due to a higher proportion of stronger titanium and increasing end plastic energy due to larger applied displacements.

The above analysis demonstrates that an optimized damper should have high stiffness under small applied displacements and have high peak forces under larger displacements. For a medium value of the applied displacement (Dsg. 3), the optimized design leverages multiple materials to strike a balance between stiffness and peak force and maximize plastic energy. We also note that, for simplicity, the case study here features a single applied displacement for each design. For designs undergoing multiple applied displacements, such as building structures in earthquake engineering (Jia et al., 2019), the current topology optimization framework can be extended to multiple load cases. Additionally, we remark that while the proposed framework employs a fixed-grid mesh during topology optimization, body-fitted meshes are typically used for manufacturing the optimized designs. However, the performance difference between optimized designs defined on these two mesh types is negligible, as demonstrated in Appendix C.

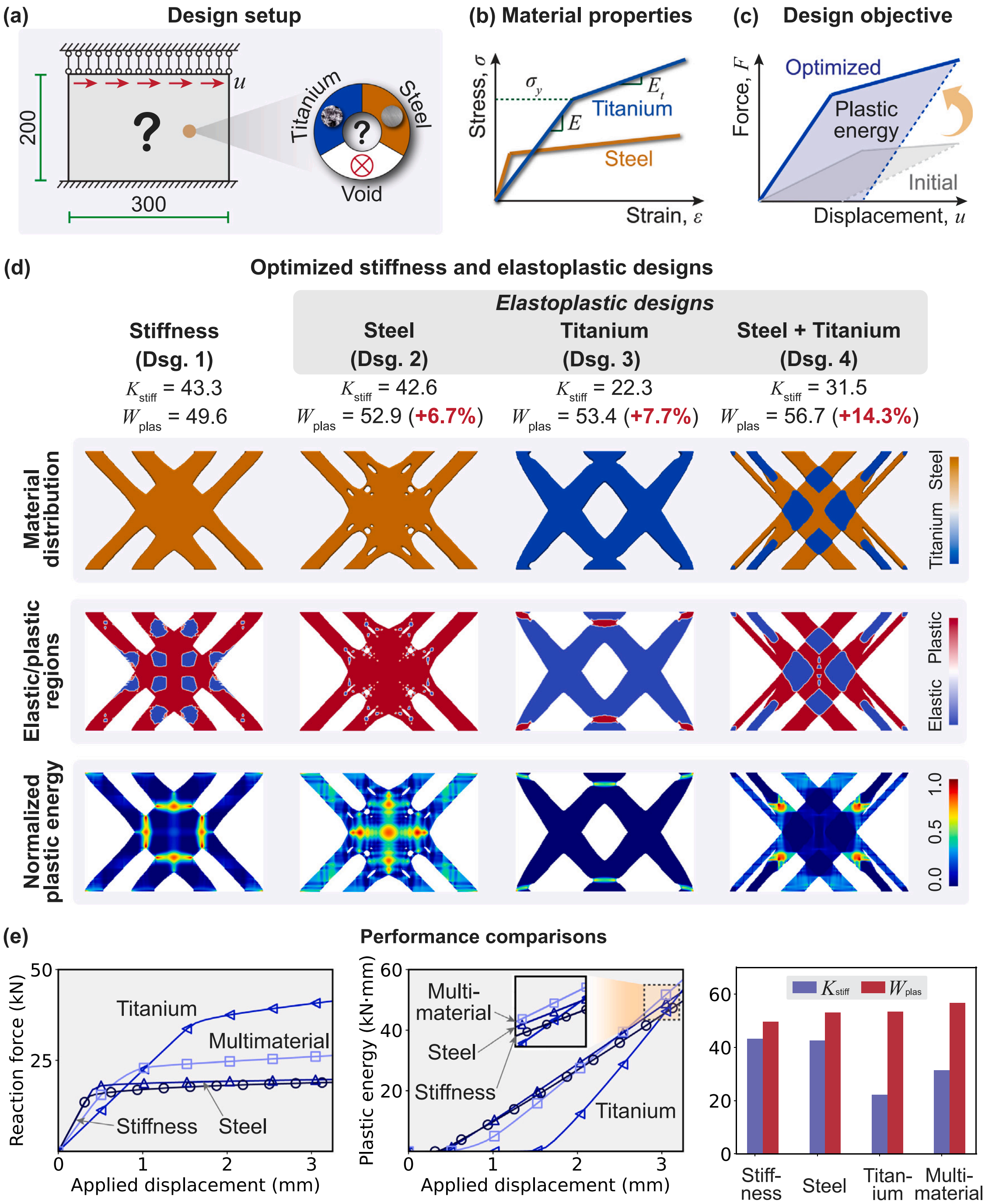

Fig. 4. Comparison of stiffness-maximization and elastoplastic designs for metallic dampers. (a) Design setup including the design domain, boundary conditions, and candidate materials (titanium, steel, and void). The geometries of the design domain are in mm. The variable u is the amplitude of the applied displacement loading. (b) The material properties of titanium and steel. The variables E, E_t, and σ_y are the Young's modulus, elastoplastic modulus, and yield strength, respectively. (c) The design objective of maximizing plastic energy. (d) Material distribution, elastic/plastic regions, and normalized plastic energy density of the optimized designs. Dsg. 1 is obtained by classical stiffness maximization. Dsgs. 2–4 are elastoplastic designs generated by the proposed approach, where Dsg. 2 is obtained by using only steel, Dsg. 3 by using only titanium, and Dsg. 4 is the multimaterial design. The variables $K_{\mathtt{stiff}}$ and $W_{\mathtt{plas}}$ are the initial stiffness (in kN/mm) and total plastic energy (in kN·mm), respectively. (e) Performance comparisons of the optimized designs.

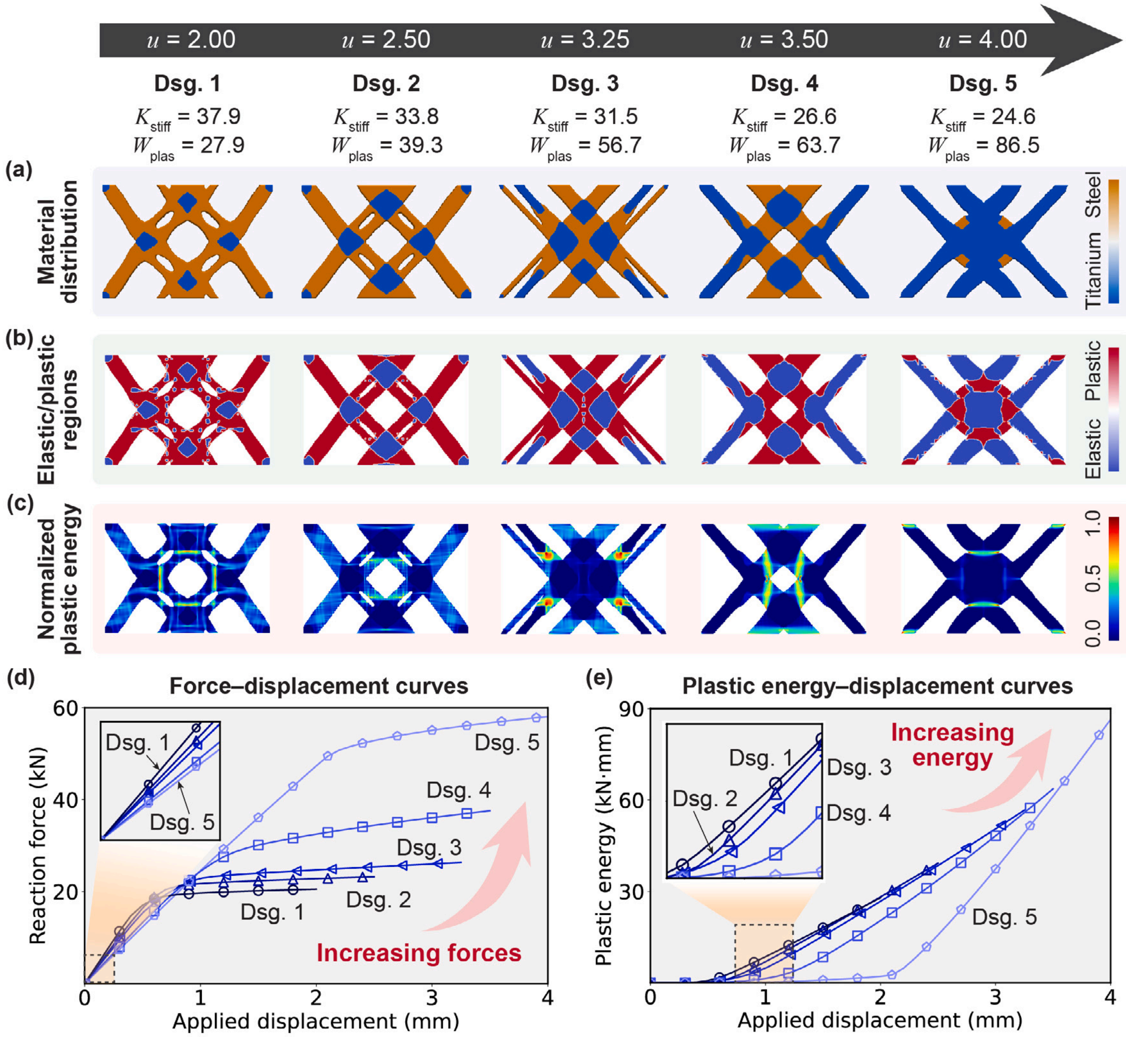

Fig. 5. Comparison among the optimized elastoplastic designs under increasing applied displacements. (a)–(c) Optimized material distribution, elastic/plastic regions, and normalized plastic energy densities. The variables $K_{\mathtt{stiff}}$ and $W_{\mathtt{plas}}$ are the initial stiffness (in kN/mm) and plastic energy (in kN·mm), respectively. (d)–(e) Force–displacement and plastic energy–displacement curves of the optimized designs.

4.2. Elastoplastic structures with optimized yield resistance

In this subsection, we focus on delaying yielding for yield-resistant structures. To achieve this goal, we consider all four energy terms ($W_{\mathtt{elas,I}}$, $W_{\mathtt{plas,I}}$, $W_{\mathtt{elas,II}}$, and $W_{\mathtt{plas,II}}$) in the objective function from (9) and use the same weights for $W_{\mathtt{elas,II}}$ and $W_{\mathtt{plas,II}}$, which reduces the objective function to

$$J = -w_{\mathtt{elas,I}} W_{\mathtt{elas,I}} + w_{\mathtt{plas,I}} W_{\mathtt{plas,I}} - w_{\mathtt{total,II}} W_{\mathtt{total,II}} \tag{10}$$

where $W_{\mathtt{total,II}} = W_{\mathtt{elas,II}} + W_{\mathtt{plas,II}}$ is the total energy in stage II, and $w_{\mathtt{total,II}}$ is the associated weighting factor subjected to $w_{\mathtt{elas,I}} + w_{\mathtt{plas,I}} + w_{\mathtt{total,II}} = 1$. This reformulated multiobjective function is akin to the one in Jia et al. (2023), which demonstrates success in designing fracture-resistant structures. In the current context, we replace the fracture energy from Jia et al. (2023) with plastic energy and examine the influence of the weighting ratios of energies ($w_{\mathtt{elas,I}} : w_{\mathtt{total,II}}$) and the critical displacement ($u_{\mathtt{crit}}$) on the optimized designs, which are laid out below.

4.2.1. Sequential yielding for preventing catastrophic failure

We begin by studying the optimized yield-resistant structures with various weighting ratios and then introduce the mechanism for preventing catastrophic failure through sequential material yielding. Fig. 6(a) shows the design setup, including the design domain, boundary conditions, and the candidate materials (titanium, steel, and void). The design domain is a disk with the same geometry as the one in Jia et al. (2023) while subjected to a superposition of prescribed rotational and biaxially tensile displacements. The amplitude of the total prescribed displacement is $\sqrt{2}u$ with $u = 0.04$ mm. Fig. 6(b) recaps the material properties of titanium and steel used here. Fig. 6(c) presents the design objectives, which include enhancing initial stiffness, delaying yielding, and maximizing total energy.

To perform topology optimization, we adopt the following FEA and optimization parameters. The design domain is discretized using an unstructured mesh containing 42,472 first-order quadrilateral elements of average size $h = 0.03$ mm. The maximum optimization iteration is 400. The critical displacement is $u_{\mathrm{crit}} = 0.004$ mm. The allowable material volume fractions are $\overline{V}_1 = \overline{V}_2 = 0.25$ for titanium and steel, respectively. The filter radii for the density and material variables are $R_\rho = R_\xi = 0.3$ mm, respectively. The Heaviside sharpness parameter for both density and material variables is $\beta = 1$ initially and doubled every 40 optimization iterations starting from iteration 41 until $\beta = 128$. The penalty parameters for the density variable are $p_\rho^E = p_\rho^K = p_\rho^H = 3$ and $p_\rho^{\sigma_y} = 2.5$. The penalty parameter for the material variable is $p_\xi = 1$ initially and increased by 0.5 every 80 optimization iterations starting from iteration 41 until $p_\xi = 3$. The move limit in the MMA optimizer is $m \in [0.1, 0.2]$. During topology optimization, we use 20 load steps in FEA with a plane strain assumption for all designs. After topology optimization, we use the same loading procedure to evaluate the elastoplastic responses of the designs.

Based on the above setups, we obtain the optimized designs and their elastoplastic responses in Fig. 6(d). Here, we set $w_{\mathrm{plas,I}} \equiv 0.7$ and investigate the influence of the $w_{\mathrm{elas,I}}$-to-$w_{\mathrm{total,II}}$ ratio on optimized designs. As illustrated in Fig. 6(d), all optimized designs share the same topology but have disparate material distributions. Specifically, when $w_{\mathrm{elas,I}}$ is larger (Dsgs. 1 and 2), the stiffer steel material constitutes the major members connecting the inner fixed end to the outer applied displacement loading. Additionally, the titanium material forms bulky joints to compensate for its lower stiffness. As $w_{\mathrm{elas,I}}$ decreases and $w_{\mathrm{total,II}}$ increases (Dsgs. 3 and 4), the stronger titanium material gradually becomes part of the major structural members to provide a higher peak force and greater total energy. Ultimately, when $w_{\mathrm{total,II}}$ reaches its maximum value ($w_{\mathrm{total,II}} = 0.3$), the major members of the optimized design are dominated by titanium.

The force–displacement and plastic energy–displacement curves of the optimized designs are shown in Fig. 6(e), from which we can observe the following. First, with a smaller $w_{\mathrm{elas,I}}$ and larger $w_{\mathrm{total,II}}$, the structural stiffness (K_{stiff}) decreases while the total energy (W_{total}) and peak force (F_{peak}) increase. This trend is because softer yet stronger titanium gradually enters the major structural components. Second, while Dsg. 1 has the highest stiffness, its force levels out as soon as the material yields, resulting in the lowest peak force and total energy. By contrast, Dsg. 4 can still carry the load even after material yielding, achieving a 156% higher peak force and 120% higher total energy compared to Dsg. 1. Meanwhile, the stiffness of Dsg. 4 is only reduced by 13% compared to Dsg. 1. This performance gain of Dsg. 4 is enabled by using a nonzero $w_{\mathrm{total,II}}$ ($w_{\mathrm{total,II}} = 0.15$ here), demonstrating the necessity of the multiobjective function in (10).

To understand the performance gain of Dsg. 4, we plot the elastic/plastic regions of both Dsgs. 1 and 4 under two applied displacements, $u = 0.006$ and $u = 0.040$ mm (insets in Fig. 6(e)). In Dsg. 1, the steel material yields at $u = 0.006$ mm and destroys the load paths from the outer applied displacement loading to the inner fixed end. This is a result of the serial arrangement of the steel and titanium materials, causing Dsg. 1 to exhibit a single yielding mode until the end of loading ($u = 0.040$ mm). Conversely, in Dsg. 4, the titanium part can still carry the load after the steel part yields at $u = 0.006$ mm, owing to the parallel arrangement of the two materials. With further loading, the titanium part eventually yields, and the entire design displays improved peak force and total energy through sequential material yielding. A complete history of the sequential yielding of the steel and titanium materials in Dsg. 4 is presented in Fig. 6(f).

The above analysis demonstrates that optimized designs achieve different stiffness–energy trade-offs through various $w_{\mathrm{elas,I}}$-to-$w_{\mathrm{total,II}}$ ratios. These trade-offs are manifested through the parallel arrangement of the stiffer yet weaker material and the stronger yet softer material to maximize total energy while maintaining sufficient initial stiffness. Such a parallel arrangement ensures sufficient redundancy in post-yielding capacity and prevents catastrophic failure of engineering structures.

We also note that, in this case study, we activate the individual material volume constraints to demonstrate the synergistic use of both materials. Through this treatment, we avoid trivial designs and ensure fair comparisons among designs with different $w_{\mathrm{elas,I}}$-to-$w_{\mathrm{total,II}}$ ratios. Practically, one might also restrict the use of individual materials based on their availability. However, we emphasize that these individual material constraints are optional (see Figs. 4 and 5.) upon the user's needs and choices.

4.2.2. Altering the load paths for delaying yielding

We now introduce another factor contributing to delayed yielding — altering the load paths — by analyzing the effect of the critical displacement, u_{crit}. Fig. 7(a) presents four yield-resistant designs with increasing u_{crit} values: 0.004, 0.010, 0.030, and 0.040 mm. All designs are optimized with $w_{\mathrm{elas,I}} : w_{\mathrm{plas,I}} : w_{\mathrm{total,II}} = 0.15 : 0.70 : 0.15$. Fig. 7(a) displays the initial stiffness (K_{stiff}), yield displacement (u_{yield}), total energy (W_{total}), and peak force (F_{peak}) of all designs. Here, the yield displacement is defined as

$$u_{\mathrm{yield}} = \underset{u_m}{\operatorname{argmax}} \frac{K(u_m) - K(u_{m+1})}{K(u_m)} \quad \text{with} \quad K(u_m) = \frac{F(u_m) - F(u_{m-1})}{u_m - u_{m-1}} \quad \text{for } m = 1, 2, \ldots, N^{\mathrm{step}} - 1, \tag{11}$$

where the variable u_m is the displacement amplitude at load step m. Variables $F(u_m)$ and $K(u_m)$ are the associated reaction force and tangential stiffness, respectively. We note that the variable u_{yield} corresponds to the applied displacement that induces the largest reduction in structural stiffness. It signifies the yielding of the entire structure, which can occur after the local material yielding (expected to be around u_{crit}).

The results in Fig. 7(a) show the following features. For $u_{\mathrm{crit}} = 0.004$ mm (Dsg. 1), the titanium and steel materials are arranged in parallel and form the major structural members, connecting the outer applied displacement loading to the inner fixed end. By

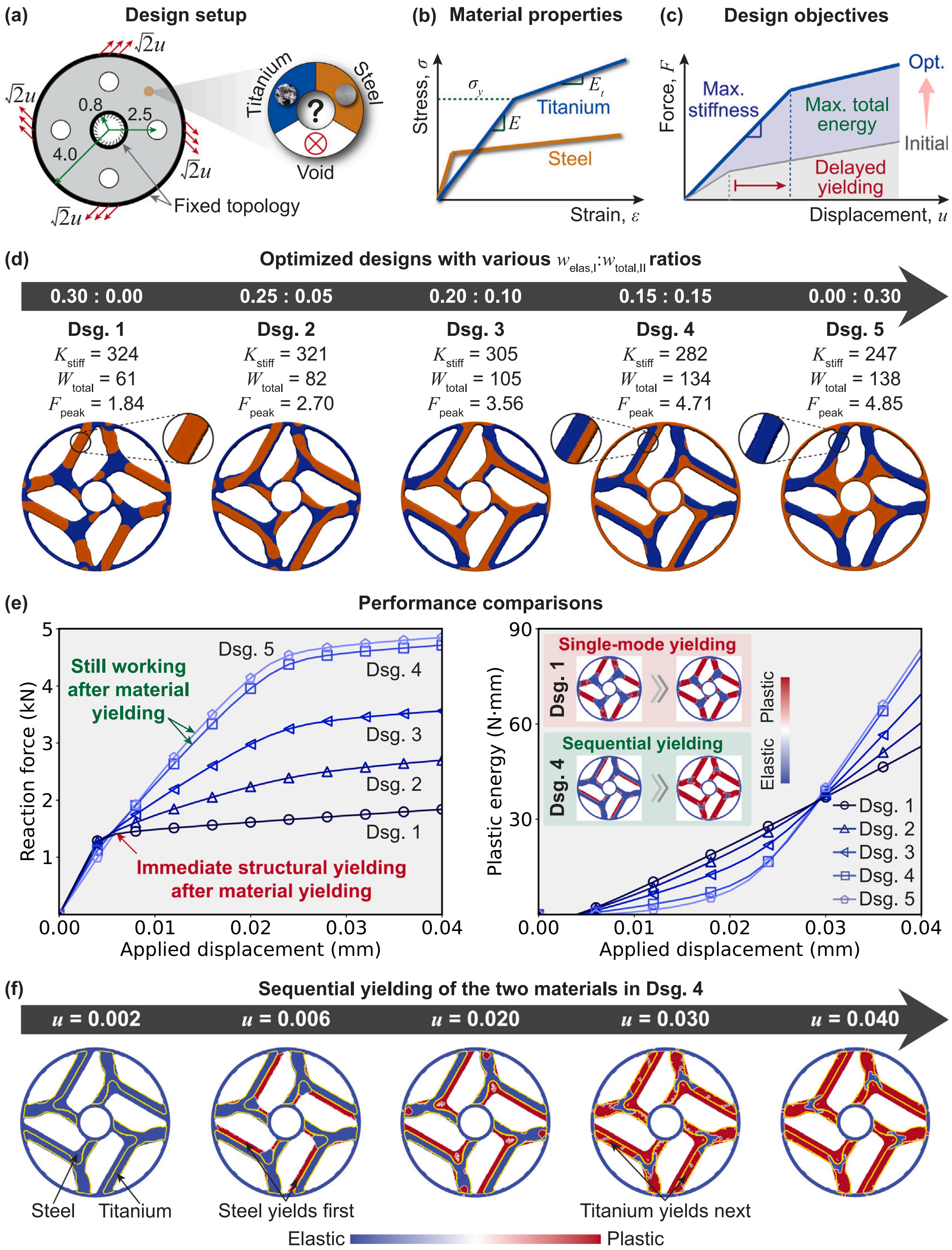

Fig. 6. Optimized yield-resistant elastoplastic designs with various weighting ratios. (a) Design setup including the design domain, boundary conditions, and the candidate materials (titanium, steel, and void). The geometries of the design domain are in mm. The variable $\sqrt{2}u$ is the amplitude of the applied displacement loading. (b) Material properties of titanium and steel. The variables E, E_t, and σ_y are Young's modulus, elastoplastic modulus, and yield strength, respectively. (c) Design objectives including maximizing initial stiffness, delaying yielding, and maximizing total energy. (d) Optimized designs with various $w_{\mathrm{elas,I}} : w_{\mathrm{total,II}}$ ratios. The variables K_{stiff}, W_{total}, and F_{peak} are the initial stiffness (in kN/mm), total energy (in N·mm), and peak force (in kN), respectively. (e) Performance comparisons of the optimized designs. (f) Sequential yielding details of the steel and titanium materials in Dsg. 4. Yellow contours indicate the material interfaces.

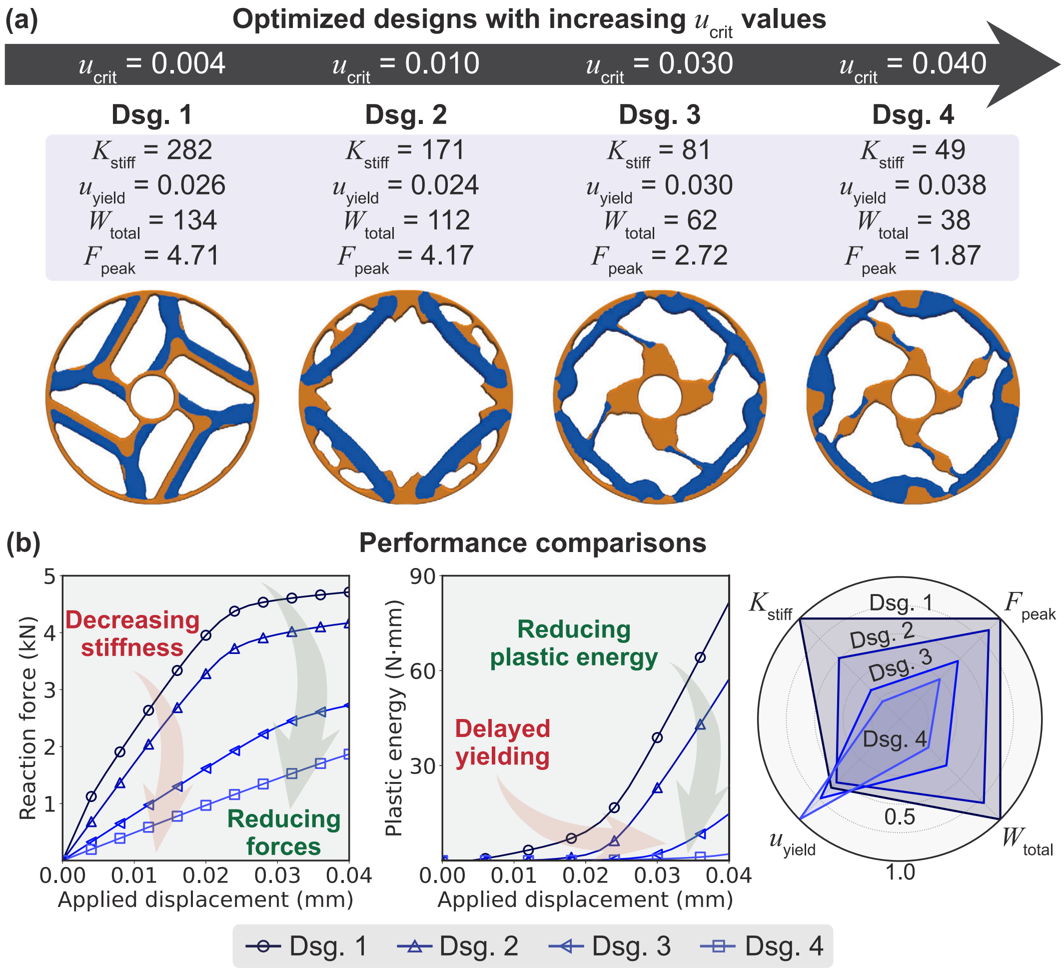

Fig. 7. Optimized yield-resistant structures with increasing u_{crit} values. (a) Optimized material distribution and performance indicators. The variables K_{stiff}, u_{yield}, W_{total}, and F_{peak} are the initial stiffness (in kN/mm), yield displacement (in mm), total energy (in N·mm), and peak force (in kN), respectively. (b) Performance comparisons of the optimized designs.

increasing the critical displacement to u_{crit} = 0.010 mm (Dsg. 2), the optimized design is detached from the inner fixed end and forms a self-equilibrium structure. Such a ring-shaped topology is known for reducing peak stress (Jia et al., 2023) and is capable of delaying yielding. As for u_{crit} = 0.030 mm (Dsg. 3) and u_{crit} = 0.040 mm (Dsg. 4), a clockwise rotating part appears in the middle and connects to the outer ring-shaped structure with slender members. Importantly, these slender members are positioned far away from the loading positions to reduce peak stress and delay yielding.

Fig. 7(b) further shows the performance comparisons of the optimized designs. The increase in u_{crit} value reduces the optimized design's stiffness and peak forces. This phenomenon is because a softer structure undergoes a lower peak stress, reducing plastic energy and delaying structural yielding. By examining the radar chart in Fig. 7(b), we observe the tradeoff among initial stiffness, yield displacement, total energy, and peak force of the optimized designs. Consequently, we can design yield-resistant structures with various target elastoplastic responses by adjusting the u_{crit} values.

4.3. Three-dimensional multi-alloy elastoplastic structures

In this final case study, we apply the proposed topology optimization framework in Section 3 to 3D. Specifically, we include a 3D stiffness-maximization design as a reference and compare it with two different elastoplastic designs: one featuring maximized total energy (by setting $w_{total,II} = 1$ and $u_{crit} = 0$) and the other emphasizing delayed yielding (by setting $w_{elas,I} : w_{plas,I} : w_{total,II} = 0.15 : 0.70 : 0.15$ and $u_{crit} = 0.8$ mm). Additionally, we demonstrate the optimized elastoplastic designs consisting of more than two candidate materials by utilizing the modified HSP in (B.1).

The detailed design setup is shown in Fig. 8(a). Here, the design domain (same as the one used in Jia et al. (2024d)) is a spherical shell with fixed top and bottom, subjected to a rotational displacement loading with an amplitude of $u = 2$ mm. We aim to determine the optimal material distribution among bronze, steel, nickel–chromium, titanium, and void. The detailed material properties are

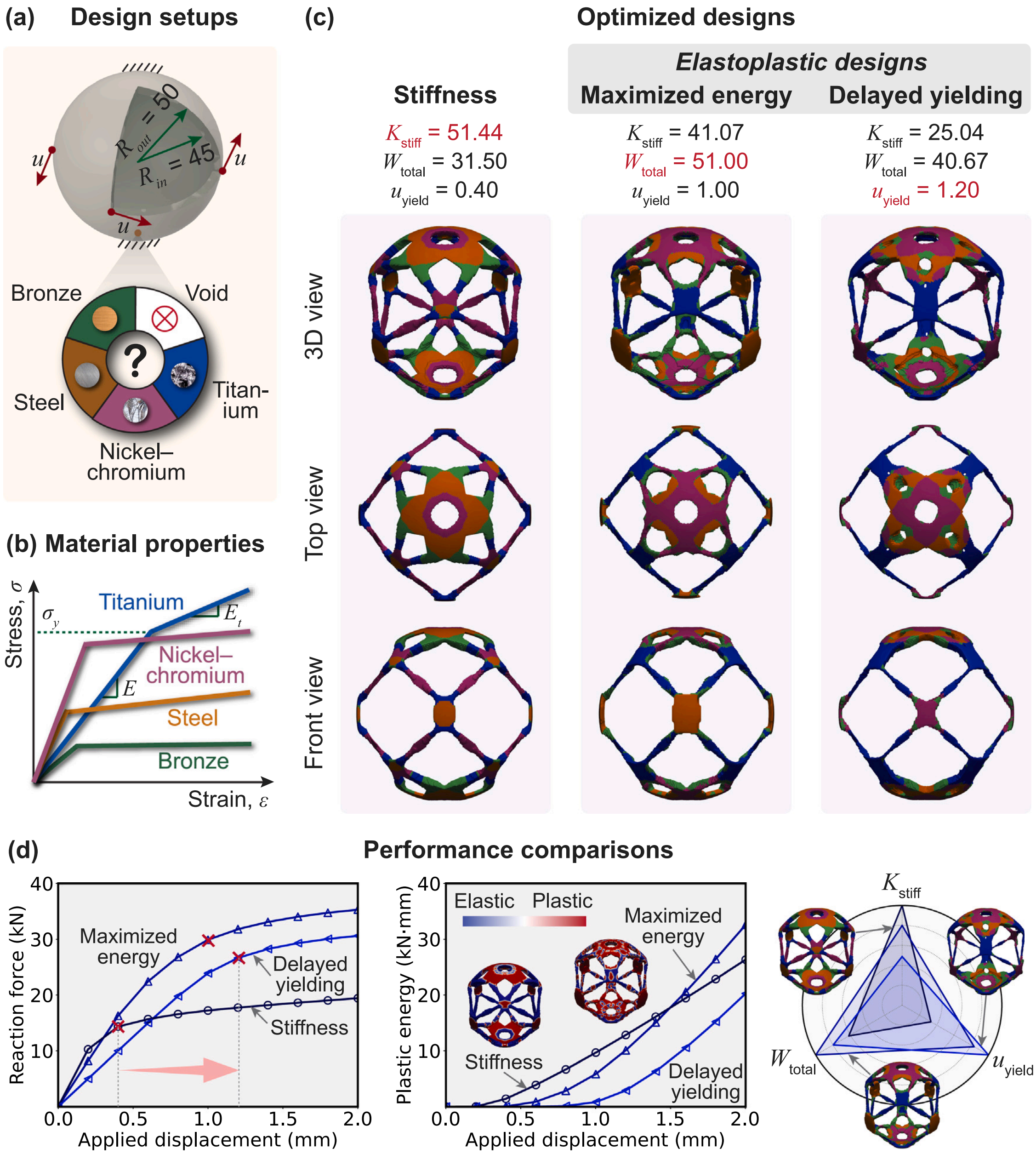

Fig. 8. Comparison of stiffness and elastoplastic designs in 3D. (a) Design setup including the design domain, boundary conditions, and candidate materials (bronze, steel, nickel–chromium, titanium, and void). The geometries of the design domain are in mm. The variable u is the amplitude of the applied displacement loading. (b) The material properties of solid candidate materials. The variables E, E_t, and σ_y are Young's modulus, elastoplastic modulus, and yield strength, respectively. (c) Optimized stiffness and elastoplastic designs. The variables $K_{\mathtt{stiff}}$, $W_{\mathtt{plas}}$, and $u_{\mathtt{yield}}$ are the initial stiffness (in kN/mm), total energy (in kN·mm), and yield displacement (in mm), respectively. (d) Performance comparisons of the optimized designs. The crosses in the force–displacement curves represent the structural yielding based on (11). The insets in the plastic energy–displacement curves show the elastic/plastic regions of the stiffness-maximization and energy-maximization designs at the final load step.

given in Table 1, and the illustrative stress–strain curves are shown in Fig. 8(b).

We use the following FEA and optimization parameters. The design domain is discretized with an unstructured mesh containing 190,080 first-order hexahedral elements of average size $h = 1.0$ mm. The maximum optimization iteration is 500. The allowable material volume fractions are $\overline{V}_1 = \overline{V}_2 = \overline{V}_3 = \overline{V}_4 = 0.04$ for the four solid candidate materials. The filter radii for the density and material variables are $R_\rho = R_\xi = 4$ mm, respectively. The Heaviside sharpness parameter for both density and material variables is $\beta = 1$ initially and doubled every 40 optimization steps beginning from iteration 41 until $\beta = 128$. The penalty parameters for the density variable are $p_\rho^E = p_\rho^K = p_\rho^H = 3$ and $p_\rho^{\sigma_y} = 2.5$. The penalty parameter for the material variable is $p_\xi = 1$ initially and increased by 0.5 every 80 optimization iterations starting from iteration 41 until $p_\xi = 3$. The move limit in the MMA optimizer is $m = 0.05$. During topology optimization, we use one load step in FEA for the stiffness-maximization design and 10 load steps for the elastoplastic designs. After topology optimization, we consistently use 10 load steps to evaluate the elastoplastic responses of all designs.

Upon topology optimization, we present the 3D, top, and front views of the optimized stiffness and elastoplastic designs in Fig. 8(c). Here, we also present the performance indicators that include initial stiffness ($K_{\mathtt{stiff}}$), total energy ($W_{\mathtt{total}}$), and yield displacement ($u_{\mathtt{yield}}$), which are summarized from the performance comparisons in Fig. 8(d). Based on Fig. 8(c)–(d), the stiffness-maximization and energy-maximization designs share similar topologies, featuring high initial stiffness by placing the stiffer materials (steel and nickel–chromium) around the areas subjected to boundary conditions. Through a non-intuitive material layout, the energy-maximization design effectively increases total energy by 61.9% (from 31.50 to 51.00 kN·mm) while reducing initial stiffness by only 20.2% (from 51.44 to 41.07 kN/mm). This increase in total energy is achieved by balancing initial stiffness and yield displacement/peak force (Fig. 8(d)), echoing the optimized designs in Fig. 5. Additionally, compared to the stiffness-maximization design, the energy-maximization structure shows more distributed plastic regions (insets in Fig. 8(d)), promoting higher plastic energy and greater total energy. Moreover, due to the trade-off between initial stiffness and peak force, the energy-maximization design exhibits a 150% improvement in yield displacement (from 0.40 to 1.00 mm).

To demonstrate explicit control of yield displacement, we present another optimized elastoplastic design with delayed yielding (the last column in Fig. 8(c)). This design shows a yield displacement of $u_{\mathtt{yield}} = 1.2$ mm, exceeding the prescribed value of $u_{\mathtt{crit}} = 0.8$ mm. To maintain a high yield displacement, this design features slender structural members that produce relatively low stress. Additionally, it delays yielding by concentrating the stronger nickel–chromium material around the areas subjected to boundary conditions. Consequently, the optimized elastoplastic design has the lowest plastic energy and highest yield displacement compared to the other two optimized structures (Fig. 8(d)).

Through this case study, we demonstrate the use of the proposed topology optimization framework to customize 3D structural elastoplastic responses, including initial stiffness, total energy, and yield displacement. These tailored behaviors are achieved by adjusting the weighting factors ($w_{\mathtt{elas,I}}$, $w_{\mathtt{plas,I}}$, and $w_{\mathtt{total,II}}$) and the critical displacement ($u_{\mathtt{crit}}$) in (10). The optimized designs reveal a balance between initial stiffness and yield displacement to achieve maximum total energy. Additionally, employing slender structural members and positioning stronger materials around the boundary conditions can effectively delay structural yielding.

5. Conclusions

In this study, we develop a multimaterial and multiobjective topology optimization approach to control various elastoplastic structural responses and reveal their underlying mechanisms. This approach simultaneously optimizes structural geometry and material phase distribution, resulting in lightweight composite structures with multiple target elastoplastic responses, including increased initial stiffness, delayed yielding, and maximized energy. To achieve these objectives, we employ a rigorous plasticity theory and the return mapping algorithm that can handle different hardening rules. Additionally, we accurately and efficiently compute history-dependent sensitivities of structural responses through a combination of the reversed adjoint method and automatic differentiation.

By leveraging the proposed optimization approach, we present three representative numerical case studies to demonstrate the discovered lightweight composite structures with optimized elastoplastic responses and the associated mechanisms. We begin by optimizing metallic yielding dampers and highlight the synergistic use of multiple materials to achieve optimal energy dissipation, where we also reveal the stiff-to-strong transition of structures under increasing applied displacements. Next, we optimize the yield resistance of the composite structures and unveil the parallel arrangement of dissimilar alloys to prevent catastrophic structural yielding. Additionally, we demonstrate that delayed yielding is realized by altering load paths and forming self-equilibrating structures. Finally, we demonstrate 3D multi-alloy structures with maximized total energy through distributed plastic regions and optimized yield resistance by placing strong materials around boundary conditions.

CRediT authorship contribution statement

Yingqi Jia: Writing – review & editing, Writing – original draft, Visualization, Validation, Software, Methodology, Investigation, Formal analysis, Data curation, Conceptualization. **Weichen Li:** Writing – review & editing, Writing – original draft, Methodology, Investigation. **Xiaojia Shelly Zhang:** Writing – review & editing, Writing – original draft, Supervision, Resources, Project administration, Methodology, Investigation, Funding acquisition, Conceptualization.

Distribution statement

Approved for public release; distribution is unlimited.

Declaration of competing interest

The authors declare that they have no known competing financial interests or personal relationships that could have appeared to influence the work reported in this paper.

Acknowledgments

Authors X.S.Z., Y.J., and W.L. would like to acknowledge the support from the U.S. Defense Advanced Research Projects Agency (DARPA) Award HR0011-24-2-0333. This material is based upon work supported by the Air Force Office of Scientific Research under award number FA9550-23-1-0297. The information provided in this paper is the sole opinion of the authors and does not necessarily reflect the view of the sponsoring agencies.

Appendix A. History-dependent sensitivity analysis and its verification

In this section, we present the history-dependent sensitivity analysis for updating the design variables (ρ and ξ_1–$\xi_{N^{\mathtt{mat}}-1}$). We start by presenting the Lagrangian expression of any objective or constraint function under consideration, along with the associated residual vectors. Next, we introduce the reversed adjoint method and automatic differentiation for accurately evaluating the history-dependent sensitivities. Lastly, we verify the sensitivity assessment by comparing it with a forward finite difference scheme.

A.1. Lagrangian expression and residual vectors

In this subsection, we introduce the Lagrangian expression of any given function of interest along with the associated residual vectors. We begin by considering a generic objective or constraint function,

$$J(\bar{\zeta};\mathbf{U}_1,\ldots,\mathbf{U}_{N^{\mathtt{step}}};\mathbf{V}^{e^p}_1,\ldots,\mathbf{V}^{e^p}_{N^{\mathtt{step}}};\mathbf{V}^{\beta}_1,\ldots,\mathbf{V}^{\beta}_{N^{\mathtt{step}}};\mathbf{V}^{\alpha}_1,\ldots,\mathbf{V}^{\alpha}_{N^{\mathtt{step}}}). \tag{A.1}$$

Here, $\bar{\zeta}$ represents the global vectors of physical variables,

$$\bar{\zeta}\in\{\bar{\rho},\bar{\xi}_1,\ldots,\bar{\xi}_{N^{\mathtt{mat}}}\}=\begin{bmatrix}\bar{\zeta}_1\\ \bar{\zeta}_2\\ \vdots\\ \bar{\zeta}_{N^{\mathtt{elem}}}\end{bmatrix}\begin{matrix}\leftarrow & \text{Element } 1\\ \leftarrow & \text{Element } 2\\ & \vdots\\ \leftarrow & \text{Element } N^{\mathtt{elem}}\end{matrix},$$

where $\bar{\zeta}_i$ is the physical variable ($\bar{\zeta}$) of finite element i, and $N^{\mathtt{elem}}$ is the number of finite elements. The variables $\mathbf{U}_1$–$\mathbf{U}_{N^{\mathtt{step}}}$ in (A.1) are global displacement vectors defined as

$$\mathbf{U}_n=\begin{bmatrix}\mathbf{u}_{n,1}\\ \mathbf{u}_{n,2}\\ \vdots\\ \mathbf{u}_{n,N^{\mathtt{node}}}\end{bmatrix}\begin{matrix}\leftarrow & \text{Node } 1\\ \leftarrow & \text{Node } 2\\ & \vdots\\ \leftarrow & \text{Node } N^{\mathtt{node}}\end{matrix}\quad\text{with}\quad \mathbf{u}_{n,i}=\begin{bmatrix}u^x_{n,i}\\ u^y_{n,i}\\ u^z_{n,i}\end{bmatrix}\quad\text{for}\quad\begin{cases}n=1,2,\ldots,N^{\mathtt{step}}\\ i=1,2,\ldots,N^{\mathtt{node}}\end{cases},$$

where $\mathbf{u}_{n,i}$ is the local displacement vector ($\mathbf{u}$) of node i at load step n, and $N^{\mathtt{node}}$ is the number of nodes. The variables $u^x_{n,i}$, $u^y_{n,i}$, and $u^z_{n,i}$ are the three components of $\mathbf{u}$ in x, y, and z directions, respectively. The variables $\mathbf{V}^{e^p}_1$–$\mathbf{V}^{e^p}_{N^{\mathtt{step}}}$ in (A.1) are global plastic strain vectors given as

$$\mathbf{V}^{e^p}_n=\begin{bmatrix}\mathbf{v}^{e^p}_{n,1}\\ \mathbf{v}^{e^p}_{n,2}\\ \vdots\\ \mathbf{v}^{e^p}_{n,N^{\mathtt{point}}}\end{bmatrix}\begin{matrix}\leftarrow & \text{Point } 1\\ \leftarrow & \text{Point } 2\\ & \vdots\\ \leftarrow & \text{Point } N^{\mathtt{point}}\end{matrix}\quad\text{with}\quad \mathbf{v}^{e^p}_{n,i}=\begin{bmatrix}(\mathbf{e}^p_{n,i})_{11}\\ (\mathbf{e}^p_{n,i})_{12}\\ (\mathbf{e}^p_{n,i})_{13}\\ (\mathbf{e}^p_{n,i})_{22}\\ (\mathbf{e}^p_{n,i})_{23}\\ (\mathbf{e}^p_{n,i})_{33}\end{bmatrix}\quad\text{for}\quad\begin{cases}n=1,2,\ldots,N^{\mathtt{step}}\\ i=1,2,\ldots,N^{\mathtt{point}}\end{cases},$$

where $\mathbf{v}^{e^p}_{n,i}$ is the local plastic strain vector ($\mathbf{v}^{e^p}$) of integration point i at load step n, whose values can be extracted from the plastic strain tensor, $\mathbf{e}^p_{n,i}$. The parameter $N^{\mathtt{point}}$ is the number of integration points. Similarly, the variables $\mathbf{V}^{\beta}_1$–$\mathbf{V}^{\beta}_{N^{\mathtt{step}}}$ in (A.1) are global back stress vectors expressed as

$$\mathbf{V}^{\beta}_n=\begin{bmatrix}\mathbf{v}^{\beta}_{n,1}\\ \mathbf{v}^{\beta}_{n,2}\\ \vdots\\ \mathbf{v}^{\beta}_{n,N^{\mathtt{point}}}\end{bmatrix}\begin{matrix}\leftarrow & \text{Point } 1\\ \leftarrow & \text{Point } 2\\ & \vdots\\ \leftarrow & \text{Point } N^{\mathtt{point}}\end{matrix}\quad\text{with}\quad \mathbf{v}^{\beta}_{n,i}=\begin{bmatrix}(\boldsymbol{\beta}_{n,i})_{11}\\ (\boldsymbol{\beta}_{n,i})_{12}\\ (\boldsymbol{\beta}_{n,i})_{13}\\ (\boldsymbol{\beta}_{n,i})_{22}\\ (\boldsymbol{\beta}_{n,i})_{23}\\ (\boldsymbol{\beta}_{n,i})_{33}\end{bmatrix}\quad\text{for}\quad\begin{cases}n=1,2,\ldots,N^{\mathtt{step}}\\ i=1,2,\ldots,N^{\mathtt{point}}\end{cases}.$$

Here, $\mathbf{v}^{\beta}_{n,i}$ is the local back stress vector ($\mathbf{v}^{\beta}$) of integration point i at load step n, whose values can be extracted from the back stress tensor, $\boldsymbol{\beta}_{n,i}$. Finally, the variables $\mathbf{V}^{\alpha}_1$–$\mathbf{V}^{\alpha}_{N^{\mathtt{step}}}$ are global vectors of the cumulative equivalent plastic strain, which are defined as

$$
\mathbf{V}_n^{\alpha} = \begin{bmatrix} \alpha_{n,1} \\ \alpha_{n,2} \\ \vdots \\ \alpha_{n,N^{\text{point}}} \end{bmatrix} \begin{matrix} \leftarrow & \text{Point } 1 \\ \leftarrow & \text{Point } 2 \\ & \vdots \\ \leftarrow & \text{Point } N^{\text{point}} \end{matrix} \quad \text{for} \quad n = 1, 2, \dots, N^{\text{step}},
$$

where $\alpha_{n,i}$ represents the cumulative equivalent plastic strain (α) of integration point i at load step n.

Based on the given function (J) in (A.1), we write out its Lagrangian expression ($\hat{J}$) as

$$
\hat{J} = J + \sum_{n=1}^{N^{\text{step}}} (\lambda_n^u \cdot \mathbf{R}_n^u + \lambda_n^{e^p} \cdot \mathbf{R}_n^{e^p} + \lambda_n^{\beta} \cdot \mathbf{R}_n^{\beta} + \lambda_n^{\alpha} \cdot \mathbf{R}_n^{\alpha}) \tag{A.2}
$$

where λ_n^u, $\lambda_n^{e^p}$, λ_n^{β}, and λ_n^{α} for $n = 1, 2, \dots, N^{\text{step}}$ are adjoint vectors to be determined. Based on the flow rules and hardening laws in (3) and the equilibrium equation in (7), the global residual vectors, $\mathbf{R}_n^u$, $\mathbf{R}_n^{e^p}$, $\mathbf{R}_n^{\beta}$, and $\mathbf{R}_n^{\alpha}$ for $n = 1, 2, \dots, N^{\text{step}}$, can be expressed as

$$
\begin{cases}
\mathbf{R}_n^u(\mathbf{U}_n, \mathbf{V}_{n-1}^{e^p}, \mathbf{V}_{n-1}^{\beta}, \mathbf{V}_{n-1}^{\alpha}) = \mathbf{F}_n^{\text{int}} - \mathbf{F}_n^{\text{ext}} = \mathbf{0} \text{ (for the free degrees of freedom)}, \\
\mathbf{R}_n^{e^p}(\mathbf{U}_n, \mathbf{V}_n^{e^p}, \mathbf{V}_{n-1}^{e^p}, \mathbf{V}_{n-1}^{\beta}, \mathbf{V}_{n-1}^{\alpha}) = \mathbf{V}_n^{e^p} - \mathbf{V}_{n-1}^{e^p} - \overline{\mathbf{V}}_n^{\Delta\gamma} \odot \mathbf{V}_n^{\mathbf{n}} = \mathbf{0}, \\
\mathbf{R}_n^{\beta}(\mathbf{U}_n, \mathbf{V}_n^{\beta}, \mathbf{V}_{n-1}^{e^p}, \mathbf{V}_{n-1}^{\beta}, \mathbf{V}_{n-1}^{\alpha}) = \mathbf{V}_n^{\beta} - \mathbf{V}_{n-1}^{\beta} - \frac{2}{3}(1-\theta)\overline{H}\, \overline{\mathbf{V}}_n^{\Delta\gamma} \odot \mathbf{V}_n^{\mathbf{n}} = \mathbf{0}, \\
\mathbf{R}_n^{\alpha}(\mathbf{U}_n, \mathbf{V}_n^{\alpha}, \mathbf{V}_{n-1}^{e^p}, \mathbf{V}_{n-1}^{\beta}, \mathbf{V}_{n-1}^{\alpha}) = \mathbf{V}_n^{\alpha} - \mathbf{V}_{n-1}^{\alpha} - \sqrt{\frac{2}{3}}\mathbf{V}_n^{\Delta\gamma} = \mathbf{0}.
\end{cases} \tag{A.3}
$$

Here, the operator $\odot$ represents the element-wise product of two vectors. The variables $\mathbf{F}_n^{\text{int}}$ and $\mathbf{F}_n^{\text{ext}}$ are global internal and external force vectors, respectively. The global vectors $\mathbf{V}_n^{\Delta\gamma}$, $\overline{\mathbf{V}}_n^{\Delta\gamma}$, and $\mathbf{V}_n^{\mathbf{n}}$ are defined as

$$
\mathbf{V}_n^{\Delta\gamma} = \begin{bmatrix} (\Delta\gamma)_{n,1} \\ (\Delta\gamma)_{n,2} \\ \vdots \\ (\Delta\gamma)_{n,N^{\text{point}}} \end{bmatrix} \begin{matrix} \leftarrow & \text{Point } 1 \\ \leftarrow & \text{Point } 2 \\ & \vdots \\ \leftarrow & \text{Point } N^{\text{point}} \end{matrix}, \quad \overline{\mathbf{V}}_n^{\Delta\gamma} = \begin{bmatrix} (\Delta\gamma)_{n,1}\mathbf{1}_{6\times1} \\ (\Delta\gamma)_{n,2}\mathbf{1}_{6\times1} \\ \vdots \\ (\Delta\gamma)_{n,N^{\text{point}}}\mathbf{1}_{6\times1} \end{bmatrix} \begin{matrix} \leftarrow & \text{Point } 1 \\ \leftarrow & \text{Point } 2 \\ & \vdots \\ \leftarrow & \text{Point } N^{\text{point}} \end{matrix},
$$

and

$$
\mathbf{V}_n^{\mathbf{n}} = \begin{bmatrix} \mathbf{v}_{n,1}^{\mathbf{n}} \\ \mathbf{v}_{n,2}^{\mathbf{n}} \\ \vdots \\ \mathbf{v}_{n,N^{\text{point}}}^{\mathbf{n}} \end{bmatrix} \begin{matrix} \leftarrow & \text{Point } 1 \\ \leftarrow & \text{Point } 2 \\ & \vdots \\ \leftarrow & \text{Point } N^{\text{point}} \end{matrix} \quad \text{with} \quad \mathbf{v}_{n,i}^{\mathbf{n}} = \begin{bmatrix} (\mathbf{n}_{n,i})_{11} \\ (\mathbf{n}_{n,i})_{12} \\ (\mathbf{n}_{n,i})_{13} \\ (\mathbf{n}_{n,i})_{22} \\ (\mathbf{n}_{n,i})_{23} \\ (\mathbf{n}_{n,i})_{33} \end{bmatrix} \quad \text{for} \quad \begin{cases} n = 1, 2, \dots, N^{\text{step}} \\ i = 1, 2, \dots, N^{\text{point}} \end{cases}.
$$

The symbol $(\Delta\gamma)_{n,i}$ represents the variable $\Delta\gamma$ of integration point i at load step n. The variable $\mathbf{v}_{n,i}^{\mathbf{n}}$ is the vector form of unit tensor ($\mathbf{n}$) of integration point i at load step n, whose values can be extracted from $\mathbf{n}_{n,i}$. The symbol $\mathbf{1}_{6\times1}$ represents a 6×1 vector with all elements equal to 1.

A.2. History-dependent sensitivity analysis

Based on the Lagrangian expression in (A.2) and global residual vectors in (A.3), we proceed to evaluate the history-dependent sensitivities by introducing the reversed adjoint method (Alberdi et al., 2018) and automatic differentiation (Margossian, 2019). By noticing

$$
\lambda_n^u \cdot \mathbf{R}_n^u = \lambda_n^{e^p} \cdot \mathbf{R}_n^{e^p} = \lambda_n^{\beta} \cdot \mathbf{R}_n^{\beta} = \lambda_n^{\alpha} \cdot \mathbf{R}_n^{\alpha} = 0 \quad \text{for} \quad n = 1, 2, \dots, N^{\text{step}},
$$

we have

$$
\begin{aligned}
\frac{\mathrm{d}J}{\mathrm{d}\overline{\zeta}} = \frac{\mathrm{d}\hat{J}}{\mathrm{d}\overline{\zeta}} = \frac{\partial J}{\partial \overline{\zeta}} &+ \sum_{n=1}^{N^{\text{step}}} \left[\left(\frac{\partial \mathbf{U}_n}{\partial \overline{\zeta}}\right)^{\top} \frac{\partial J}{\partial \mathbf{U}_n} + \left(\frac{\partial \mathbf{V}_n^{e^p}}{\partial \overline{\zeta}}\right)^{\top} \frac{\partial J}{\partial \mathbf{V}_n^{e^p}} + \left(\frac{\partial \mathbf{V}_n^{\beta}}{\partial \overline{\zeta}}\right)^{\top} \frac{\partial J}{\partial \mathbf{V}_n^{\beta}} + \left(\frac{\partial \mathbf{V}_n^{\alpha}}{\partial \overline{\zeta}}\right)^{\top} \frac{\partial J}{\partial \mathbf{V}_n^{\alpha}} \right] \\
&+ \sum_{n=1}^{N^{\text{step}}} \left[\left(\frac{\partial \mathbf{R}_n^u}{\partial \overline{\zeta}}\right)^{\top} + \left(\frac{\partial \mathbf{U}_n}{\partial \overline{\zeta}}\right)^{\top} \left(\frac{\partial \mathbf{R}_n^u}{\partial \mathbf{U}_n}\right)^{\top} + \left(\frac{\partial \mathbf{V}_{n-1}^{e^p}}{\partial \overline{\zeta}}\right)^{\top} \left(\frac{\partial \mathbf{R}_n^u}{\partial \mathbf{V}_{n-1}^{e^p}}\right)^{\top} \right. \\
&\left. + \left(\frac{\partial \mathbf{V}_{n-1}^{\beta}}{\partial \overline{\zeta}}\right)^{\top} \left(\frac{\partial \mathbf{R}_n^u}{\partial \mathbf{V}_{n-1}^{\beta}}\right)^{\top} + \left(\frac{\partial \mathbf{V}_{n-1}^{\alpha}}{\partial \overline{\zeta}}\right)^{\top} \left(\frac{\partial \mathbf{R}_n^u}{\partial \mathbf{V}_{n-1}^{\alpha}}\right)^{\top} \right] \lambda_n^u \\
&+ \sum_{n=1}^{N^{\text{step}}} \left[\left(\frac{\partial \mathbf{R}_n^{e^p}}{\partial \overline{\zeta}}\right)^{\top} + \left(\frac{\partial \mathbf{U}_n}{\partial \overline{\zeta}}\right)^{\top} \left(\frac{\partial \mathbf{R}_n^{e^p}}{\partial \mathbf{U}_n}\right)^{\top} + \left(\frac{\partial \mathbf{V}_n^{e^p}}{\partial \overline{\zeta}}\right)^{\top} \left(\frac{\partial \mathbf{R}_n^{e^p}}{\partial \mathbf{V}_n^{e^p}}\right)^{\top} \right.
\end{aligned}
$$

$$
\begin{aligned}
&+ \left(\frac{\partial \mathbf{V}^{e^p}_{n-1}}{\partial \overline{\zeta}}\right)^\top \left(\frac{\partial \mathbf{R}^{e^p}_{n}}{\partial \mathbf{V}^{e^p}_{n-1}}\right)^\top + \left(\frac{\partial \mathbf{V}^{\beta}_{n-1}}{\partial \overline{\zeta}}\right)^\top \left(\frac{\partial \mathbf{R}^{e^p}_{n}}{\partial \mathbf{V}^{\beta}_{n-1}}\right)^\top + \left(\frac{\partial \mathbf{V}^{\alpha}_{n-1}}{\partial \overline{\zeta}}\right)^\top \left(\frac{\partial \mathbf{R}^{e^p}_{n}}{\partial \mathbf{V}^{\alpha}_{n-1}}\right)^\top \Bigg] \lambda^{e^p}_n \\
&+ \sum_{n=1}^{N^{\text{step}}} \Bigg[\left(\frac{\partial \mathbf{R}^{\beta}_{n}}{\partial \overline{\zeta}}\right)^\top + \left(\frac{\partial \mathbf{U}_{n}}{\partial \overline{\zeta}}\right)^\top \left(\frac{\partial \mathbf{R}^{\beta}_{n}}{\partial \mathbf{U}_{n}}\right)^\top + \left(\frac{\partial \mathbf{V}^{\beta}_{n}}{\partial \overline{\zeta}}\right)^\top \left(\frac{\partial \mathbf{R}^{\beta}_{n}}{\partial \mathbf{V}^{\beta}_{n}}\right)^\top \\
&+ \left(\frac{\partial \mathbf{V}^{e^p}_{n-1}}{\partial \overline{\zeta}}\right)^\top \left(\frac{\partial \mathbf{R}^{\beta}_{n}}{\partial \mathbf{V}^{e^p}_{n-1}}\right)^\top + \left(\frac{\partial \mathbf{V}^{\beta}_{n-1}}{\partial \overline{\zeta}}\right)^\top \left(\frac{\partial \mathbf{R}^{\beta}_{n}}{\partial \mathbf{V}^{\beta}_{n-1}}\right)^\top + \left(\frac{\partial \mathbf{V}^{\alpha}_{n-1}}{\partial \overline{\zeta}}\right)^\top \left(\frac{\partial \mathbf{R}^{\beta}_{n}}{\partial \mathbf{V}^{\alpha}_{n-1}}\right)^\top \Bigg] \lambda^{\beta}_n \\
&+ \sum_{n=1}^{N^{\text{step}}} \Bigg[\left(\frac{\partial \mathbf{R}^{\alpha}_{n}}{\partial \overline{\zeta}}\right)^\top + \left(\frac{\partial \mathbf{U}_{n}}{\partial \overline{\zeta}}\right)^\top \left(\frac{\partial \mathbf{R}^{\alpha}_{n}}{\partial \mathbf{U}_{n}}\right)^\top + \left(\frac{\partial \mathbf{V}^{\alpha}_{n}}{\partial \overline{\zeta}}\right)^\top \left(\frac{\partial \mathbf{R}^{\alpha}_{n}}{\partial \mathbf{V}^{\alpha}_{n}}\right)^\top \\
&+ \left(\frac{\partial \mathbf{V}^{e^p}_{n-1}}{\partial \overline{\zeta}}\right)^\top \left(\frac{\partial \mathbf{R}^{\alpha}_{n}}{\partial \mathbf{V}^{e^p}_{n-1}}\right)^\top + \left(\frac{\partial \mathbf{V}^{\beta}_{n-1}}{\partial \overline{\zeta}}\right)^\top \left(\frac{\partial \mathbf{R}^{\alpha}_{n}}{\partial \mathbf{V}^{\beta}_{n-1}}\right)^\top + \left(\frac{\partial \mathbf{V}^{\alpha}_{n-1}}{\partial \overline{\zeta}}\right)^\top \left(\frac{\partial \mathbf{R}^{\alpha}_{n}}{\partial \mathbf{V}^{\alpha}_{n-1}}\right)^\top \Bigg] \lambda^{\alpha}_n.
\end{aligned}
$$

Regrouping terms yields

$$
\begin{aligned}
\frac{\mathrm{d}J}{\mathrm{d}\overline{\zeta}} &= \frac{\partial J}{\partial \overline{\zeta}} + \sum_{n=1}^{N^{\text{step}}} \left[\left(\frac{\partial \mathbf{R}^{u}_{n}}{\partial \overline{\zeta}}\right)^\top \lambda^{u}_n + \left(\frac{\partial \mathbf{R}^{e^p}_{n}}{\partial \overline{\zeta}}\right)^\top \lambda^{e^p}_n + \left(\frac{\partial \mathbf{R}^{\beta}_{n}}{\partial \overline{\zeta}}\right)^\top \lambda^{\beta}_n + \left(\frac{\partial \mathbf{R}^{\alpha}_{n}}{\partial \overline{\zeta}}\right)^\top \lambda^{\alpha}_n \right] \\
&+ \sum_{n=1}^{N^{\text{step}}} \left(\frac{\partial \mathbf{U}_{n}}{\partial \overline{\zeta}}\right)^\top \left[\frac{\partial J}{\partial \mathbf{U}_n} + \left(\frac{\partial \mathbf{R}^{u}_{n}}{\partial \mathbf{U}_{n}}\right)^\top \lambda^{u}_n + \left(\frac{\partial \mathbf{R}^{e^p}_{n}}{\partial \mathbf{U}_{n}}\right)^\top \lambda^{e^p}_n + \left(\frac{\partial \mathbf{R}^{\beta}_{n}}{\partial \mathbf{U}_{n}}\right)^\top \lambda^{\beta}_n + \left(\frac{\partial \mathbf{R}^{\alpha}_{n}}{\partial \mathbf{U}_{n}}\right)^\top \lambda^{\alpha}_n \right] \\
&+ \left(\frac{\partial \mathbf{V}^{e^p}_{N^{\text{step}}}}{\partial \overline{\zeta}}\right)^\top \left[\frac{\partial J}{\partial \mathbf{V}^{e^p}_{N^{\text{step}}}} + \left(\frac{\partial \mathbf{R}^{e^p}_{N^{\text{step}}}}{\partial \mathbf{V}^{e^p}_{N^{\text{step}}}}\right)^\top \lambda^{e^p}_{N^{\text{step}}} \right] \\
&+ \left(\frac{\partial \mathbf{V}^{\beta}_{N^{\text{step}}}}{\partial \overline{\zeta}}\right)^\top \left[\frac{\partial J}{\partial \mathbf{V}^{\beta}_{N^{\text{step}}}} + \left(\frac{\partial \mathbf{R}^{\beta}_{N^{\text{step}}}}{\partial \mathbf{V}^{\beta}_{N^{\text{step}}}}\right)^\top \lambda^{\beta}_{N^{\text{step}}} \right] \\
&+ \left(\frac{\partial \mathbf{V}^{\alpha}_{N^{\text{step}}}}{\partial \overline{\zeta}}\right)^\top \left[\frac{\partial J}{\partial \mathbf{V}^{\alpha}_{N^{\text{step}}}} + \left(\frac{\partial \mathbf{R}^{\alpha}_{N^{\text{step}}}}{\partial \mathbf{V}^{\alpha}_{N^{\text{step}}}}\right)^\top \lambda^{\alpha}_{N^{\text{step}}} \right] \\
&+ \sum_{n=1}^{N^{\text{step}}-1} \left(\frac{\partial \mathbf{V}^{e^p}_{n}}{\partial \overline{\zeta}}\right)^\top \Bigg[\frac{\partial J}{\partial \mathbf{V}^{e^p}_n} + \left(\frac{\partial \mathbf{R}^{e^p}_{n}}{\partial \mathbf{V}^{e^p}_{n}}\right)^\top \lambda^{e^p}_n + \left(\frac{\partial \mathbf{R}^{u}_{n+1}}{\partial \mathbf{V}^{e^p}_{n}}\right)^\top \lambda^{u}_{n+1} + \left(\frac{\partial \mathbf{R}^{e^p}_{n+1}}{\partial \mathbf{V}^{e^p}_{n}}\right)^\top \lambda^{e^p}_{n+1} \\
&+ \left(\frac{\partial \mathbf{R}^{\beta}_{n+1}}{\partial \mathbf{V}^{e^p}_{n}}\right)^\top \lambda^{\beta}_{n+1} + \left(\frac{\partial \mathbf{R}^{\alpha}_{n+1}}{\partial \mathbf{V}^{e^p}_{n}}\right)^\top \lambda^{\alpha}_{n+1} \Bigg] \\
&+ \sum_{n=1}^{N^{\text{step}}-1} \left(\frac{\partial \mathbf{V}^{\beta}_{n}}{\partial \overline{\zeta}}\right)^\top \Bigg[\frac{\partial J}{\partial \mathbf{V}^{\beta}_n} + \left(\frac{\partial \mathbf{R}^{\beta}_{n}}{\partial \mathbf{V}^{\beta}_{n}}\right)^\top \lambda^{\beta}_n + \left(\frac{\partial \mathbf{R}^{u}_{n+1}}{\partial \mathbf{V}^{\beta}_{n}}\right)^\top \lambda^{u}_{n+1} + \left(\frac{\partial \mathbf{R}^{e^p}_{n+1}}{\partial \mathbf{V}^{\beta}_{n}}\right)^\top \lambda^{e^p}_{n+1} \\
&+ \left(\frac{\partial \mathbf{R}^{\beta}_{n+1}}{\partial \mathbf{V}^{\beta}_{n}}\right)^\top \lambda^{\beta}_{n+1} + \left(\frac{\partial \mathbf{R}^{\alpha}_{n+1}}{\partial \mathbf{V}^{\beta}_{n}}\right)^\top \lambda^{\alpha}_{n+1} \Bigg] \\
&+ \sum_{n=1}^{N^{\text{step}}-1} \left(\frac{\partial \mathbf{V}^{\alpha}_{n}}{\partial \overline{\zeta}}\right)^\top \Bigg[\frac{\partial J}{\partial \mathbf{V}^{\alpha}_n} + \left(\frac{\partial \mathbf{R}^{\alpha}_{n}}{\partial \mathbf{V}^{\alpha}_{n}}\right)^\top \lambda^{\alpha}_n + \left(\frac{\partial \mathbf{R}^{u}_{n+1}}{\partial \mathbf{V}^{\alpha}_{n}}\right)^\top \lambda^{u}_{n+1} + \left(\frac{\partial \mathbf{R}^{e^p}_{n+1}}{\partial \mathbf{V}^{\alpha}_{n}}\right)^\top \lambda^{e^p}_{n+1} \\
&+ \left(\frac{\partial \mathbf{R}^{\beta}_{n+1}}{\partial \mathbf{V}^{\alpha}_{n}}\right)^\top \lambda^{\beta}_{n+1} + \left(\frac{\partial \mathbf{R}^{\alpha}_{n+1}}{\partial \mathbf{V}^{\alpha}_{n}}\right)^\top \lambda^{\alpha}_{n+1} \Bigg]
\end{aligned}
$$

according to

$$
\frac{\partial \mathbf{V}^{e^p}_0}{\partial \overline{\zeta}} = \frac{\partial \mathbf{V}^{\beta}_0}{\partial \overline{\zeta}} = \frac{\partial \mathbf{V}^{\alpha}_0}{\partial \overline{\zeta}} = \mathbf{0}.
$$

To eliminate the computationally expensive terms of $\partial \mathbf{U}_n/\partial\overline{\zeta}$, $\partial \mathbf{V}^{e^p}_n/\partial\overline{\zeta}$, $\partial \mathbf{V}^{\beta}_n/\partial\overline{\zeta}$, and $\partial \mathbf{V}^{\alpha}_n/\partial\overline{\zeta}$, we set their coefficients to be zero and derive a procedure for solving the adjoint vectors, λ^u_n, $\lambda^{e^p}_n$, λ^{β}_n, and λ^{α}_n for load steps $n = N^{\text{step}}, N^{\text{step}} - 1, \ldots, 1$, in a reversed order. Specifically, for load step N^{step}, we have

$$\begin{cases} \lambda^{e^p}_{N^{\text{step}}} = -\dfrac{\partial J_{N^{\text{step}}}}{\partial \mathbf{V}^{e^p}_{N^{\text{step}}}}, \quad \lambda^{\beta}_{N^{\text{step}}} = -\dfrac{\partial J_{N^{\text{step}}}}{\partial \mathbf{V}^{\beta}_{N^{\text{step}}}}, \quad \lambda^{\alpha}_{N^{\text{step}}} = -\dfrac{\partial J_{N^{\text{step}}}}{\partial \mathbf{V}^{\alpha}_{N^{\text{step}}}}, \\ \left(\dfrac{\partial \mathbf{R}^u_{N^{\text{step}}}}{\partial \mathbf{U}_{N^{\text{step}}}}\right)^{\top} \lambda^u_{N^{\text{step}}} = -\left[\dfrac{\partial J_{N^{\text{step}}}}{\partial \mathbf{U}_{N^{\text{step}}}} + \left(\dfrac{\partial \mathbf{R}^{e^p}_{N^{\text{step}}}}{\partial \mathbf{U}_{N^{\text{step}}}}\right)^{\top} \lambda^{e^p}_{N^{\text{step}}} + \left(\dfrac{\partial \mathbf{R}^{\beta}_{N^{\text{step}}}}{\partial \mathbf{U}_{N^{\text{step}}}}\right)^{\top} \lambda^{\beta}_{N^{\text{step}}} + \left(\dfrac{\partial \mathbf{R}^{\alpha}_{N^{\text{step}}}}{\partial \mathbf{U}_{N^{\text{step}}}}\right)^{\top} \lambda^{\alpha}_{N^{\text{step}}}\right]. \end{cases}$$

For load step $n \in \{N^{\text{step}}-1, N^{\text{step}}-2, \dots, 1\}$, we have

$$\begin{cases} \lambda^{e^p}_n = -\left[\dfrac{\partial (J_n + J_{n+1})}{\partial \mathbf{V}^{e^p}_n} + \left(\dfrac{\partial \mathbf{R}^u_{n+1}}{\partial \mathbf{V}^{e^p}_n}\right)^{\top} \lambda^u_{n+1} + \left(\dfrac{\partial \mathbf{R}^{e^p}_{n+1}}{\partial \mathbf{V}^{e^p}_n}\right)^{\top} \lambda^{e^p}_{n+1} + \left(\dfrac{\partial \mathbf{R}^{\beta}_{n+1}}{\partial \mathbf{V}^{e^p}_n}\right)^{\top} \lambda^{\beta}_{n+1} + \left(\dfrac{\partial \mathbf{R}^{\alpha}_{n+1}}{\partial \mathbf{V}^{e^p}_n}\right)^{\top} \lambda^{\alpha}_{n+1}\right], \\ \lambda^{\beta}_n = -\left[\dfrac{\partial (J_n + J_{n+1})}{\partial \mathbf{V}^{\beta}_n} + \left(\dfrac{\partial \mathbf{R}^u_{n+1}}{\partial \mathbf{V}^{\beta}_n}\right)^{\top} \lambda^u_{n+1} + \left(\dfrac{\partial \mathbf{R}^{e^p}_{n+1}}{\partial \mathbf{V}^{\beta}_n}\right)^{\top} \lambda^{e^p}_{n+1} \left(\dfrac{\partial \mathbf{R}^{\beta}_{n+1}}{\partial \mathbf{V}^{\beta}_n}\right)^{\top} \lambda^{\beta}_{n+1} + \left(\dfrac{\partial \mathbf{R}^{\alpha}_{n+1}}{\partial \mathbf{V}^{\beta}_n}\right)^{\top} \lambda^{\alpha}_{n+1}\right], \\ \lambda^{\alpha}_n = -\left[\dfrac{\partial (J_n + J_{n+1})}{\partial \mathbf{V}^{\alpha}_n} + \left(\dfrac{\partial \mathbf{R}^u_{n+1}}{\partial \mathbf{V}^{\alpha}_n}\right)^{\top} \lambda^u_{n+1} + \left(\dfrac{\partial \mathbf{R}^{e^p}_{n+1}}{\partial \mathbf{V}^{\alpha}_n}\right)^{\top} \lambda^{e^p}_{n+1} + \left(\dfrac{\partial \mathbf{R}^{\beta}_{n+1}}{\partial \mathbf{V}^{\alpha}_n}\right)^{\top} \lambda^{\beta}_{n+1} + \left(\dfrac{\partial \mathbf{R}^{\alpha}_{n+1}}{\partial \mathbf{V}^{\alpha}_n}\right)^{\top} \lambda^{\alpha}_{n+1}\right], \\ \left(\dfrac{\partial \mathbf{R}^u_n}{\partial \mathbf{U}_n}\right)^{\top} \lambda^u_n = -\left[\dfrac{\partial (J_n + J_{n+1})}{\partial \mathbf{U}_n} + \left(\dfrac{\partial \mathbf{R}^{e^p}_n}{\partial \mathbf{U}_n}\right)^{\top} \lambda^{e^p}_n + \left(\dfrac{\partial \mathbf{R}^{\beta}_n}{\partial \mathbf{U}_n}\right)^{\top} \lambda^{\beta}_n + \left(\dfrac{\partial \mathbf{R}^{\alpha}_n}{\partial \mathbf{U}_n}\right)^{\top} \lambda^{\alpha}_n\right]. \end{cases}$$

To derive the adjoint vectors in these expressions, we utilize the fact that

$$\frac{\partial \mathbf{R}^{e^p}_n}{\partial \mathbf{V}^{e^p}_n} = \frac{\partial \mathbf{R}^{\beta}_n}{\partial \mathbf{V}^{\beta}_n} = \frac{\partial \mathbf{R}^{\alpha}_n}{\partial \mathbf{V}^{\alpha}_n} = \mathbf{I} \quad \text{for} \quad n = 1, 2, \dots, N^{\text{step}}$$

and also expand the generic function J as

$$J = \sum_{n=1}^{N^{\text{step}}} J_n(\bar{\zeta}; \mathbf{U}_n, \mathbf{V}^{e^p}_n, \mathbf{V}^{\beta}_n, \mathbf{V}^{\alpha}_n; \mathbf{U}_{n-1}, \mathbf{V}^{e^p}_{n-1}, \mathbf{V}^{\beta}_{n-1}, \mathbf{V}^{\alpha}_{n-1}).$$

One obvious next step is to compute the partial derivatives involved in these expressions. Unlike Alberdi et al. (2018), which explicitly solve all the partial derivatives, we leverage automatic differentiation (Margossian, 2019) to avoid the tedious hand derivations of complex chain rules. This technique exploits the fact that any complex computer calculation can be decomposed into a series of elementary algorithmic operations and functions. To evaluate the sensitivity of a complex function, we can repeatedly apply the chain rules associated with these elementary operations and functions. Recently, this automatic differentiation technique has been widely employed in modern computational packages, including FEniCSx (Baratta et al., 2023), JAX (Bradbury et al., 2018), and PyTorch (Paszke et al., 2019). In this work, we employ FEniTop (Jia et al., 2024d) (built upon FEniCSx) to evaluate the partial derivatives using automatic differentiation.

Once the associated partial derivatives are computed, we can express the sensitivity of any generic function (J) as

$$\frac{\mathrm{d}J}{\mathrm{d}\bar{\zeta}} = \frac{\partial J}{\partial \bar{\zeta}} + \sum_{n=1}^{N^{\text{step}}} \left[\left(\frac{\partial \mathbf{R}^u_n}{\partial \bar{\zeta}}\right)^{\top} \lambda^u_n + \left(\frac{\partial \mathbf{R}^{e^p}_n}{\partial \bar{\zeta}}\right)^{\top} \lambda^{e^p}_n + \left(\frac{\partial \mathbf{R}^{\beta}_n}{\partial \bar{\zeta}}\right)^{\top} \lambda^{\beta}_n + \left(\frac{\partial \mathbf{R}^{\alpha}_n}{\partial \bar{\zeta}}\right)^{\top} \lambda^{\alpha}_n\right]. \tag{A.4}$$

Note that the sensitivity expression in (A.4) pertains to the physical variables ($\bar{\zeta}$). To compute the sensitivities with respect to the design variables (ζ), we can apply the chain rule to (A.4), incorporating the sensitivities of the linear filter (Talischi et al., 2012), Heaviside projection (Ferrari and Sigmund, 2020), and HSP (Zhou et al., 2018). The above history-dependent sensitivity analysis is summarized in Algorithm 3.

A.3. Sensitivity verification

In this subsection, we verify the sensitivity evaluation described in A.2 by comparing it with the forward finite difference scheme. For a given function, J, the finite difference method approximates its sensitivity as

$$\frac{\mathrm{d}J}{\mathrm{d}\zeta} = \frac{J(\zeta + \varepsilon) - J(\zeta)}{\varepsilon_{\mathtt{fd}}} \quad \text{for} \quad \zeta \in \{\rho, \xi_1, \xi_2, \dots, \xi_{N^{\mathtt{mat}}-1}\}.$$

Here, the symbols $\boldsymbol{\rho}$ and $\boldsymbol{\xi}_1$–$\boldsymbol{\xi}_{N^{\mathtt{mat}}-1}$ represent global vectors of design variables, ρ and ξ_1–$\xi_{N^{\mathtt{mat}}-1}$, respectively. The perturbation parameter, $\varepsilon_{\mathtt{fd}} = 10^{-5}$, is chosen to balance truncation and rounding errors. The perturbation vector, $\boldsymbol{\varepsilon}$, is defined such that $\varepsilon_i = \varepsilon_{\mathtt{fd}}$ if the design variable of finite element i is being checked and $\varepsilon_i = 0$ otherwise.

To verify the sensitivity analysis in A.2, we use Dsg. 4 from Fig. 6(d) as a case study and compare the sensitivities obtained from both approaches. As shown in Fig. A.9, we evaluate several functions, including elastic energy in stage I ($W_{\mathtt{elas,I}}$), plastic energy in stage I ($W_{\mathtt{plas,I}}$), total energy in stage II ($W_{\mathtt{total,II}}$), and volume fractions of materials 1 and 2 (g_1 and g_2, respectively). The comparison reveals a strong agreement between the sensitivities obtained from the two methods, as evidenced by the negligible absolute and relative 2-norm errors for each function.

Algorithm 3: History-dependent sensitivity analysis for small deformation elastoplasticity

Inputs: global vectors of the displacement ($\mathbf{U}_n$), plastic strain ($\mathbf{V}_n^{e^p}$), back stress ($\mathbf{V}_n^{\beta}$), and cumulative equivalent plastic strain ($\mathbf{V}_n^{\alpha}$) where $n = 1, 2, \ldots, N^{\mathtt{step}}$;
Initialization: load step counter, $n \leftarrow N^{\mathtt{step}}$; sensitivity, $\mathrm{d}J/\mathrm{d}\overline{\zeta} \leftarrow \partial J/\partial\overline{\zeta}$;
while $n \geq 1$ **do**
  Compute the partial derivatives of $\partial J_n/\partial \mathbf{W}_n$ for $\mathbf{W}_n \in \{\mathbf{U}_n, \mathbf{V}_n^{e^p}, \mathbf{V}_n^{\beta}, \mathbf{V}_n^{\alpha}\}$;
  Compute the partial derivatives of $\partial \mathbf{R}_n^{\phi}/\partial \mathbf{U}_n$ for $\phi \in \{u, e^p, \beta, \alpha\}$;
  if $n < N^{step}$ **then**
    Compute the partial derivatives of $\partial J_{n+1}/\partial \mathbf{W}_n$ for $\mathbf{W}_n \in \{\mathbf{U}_n, \mathbf{V}_n^{e^p}, \mathbf{V}_n^{\beta}, \mathbf{V}_n^{\alpha}\}$;
    Compute the partial derivatives of $\partial \mathbf{R}_{n+1}^{\phi}/\partial \mathbf{W}_n$ for $\phi \in \{u, e^p, \beta, \alpha\}$ and $\mathbf{W}_n \in \{\mathbf{V}_n^{e^p}, \mathbf{V}_n^{\beta}, \mathbf{V}_n^{\alpha}\}$;
  end
  Compute the adjoint vectors of λ_n^{ϕ} for $\phi \in \{u, e^p, \beta, \alpha\}$;
  Compute the partial derivatives of $\partial \mathbf{R}_n^{\phi}/\partial\overline{\zeta}$ for $\phi \in \{u, e^p, \beta, \alpha\}$;
  Update the sensitivity as $\mathrm{d}J/\mathrm{d}\overline{\zeta} \leftarrow \mathrm{d}J/\mathrm{d}\overline{\zeta} + \sum_{\phi\in\{u,e^p,\beta,\alpha\}} (\partial \mathbf{R}_n^{\phi}/\partial\overline{\zeta})^{\top} \lambda_n^{\phi}$;
  Update the load step counter as $n \leftarrow n - 1$;
end
Convert the sensitivity of $\mathrm{d}J/\mathrm{d}\overline{\zeta}$ to $\mathrm{d}J/\mathrm{d}\zeta$ with chain rules;

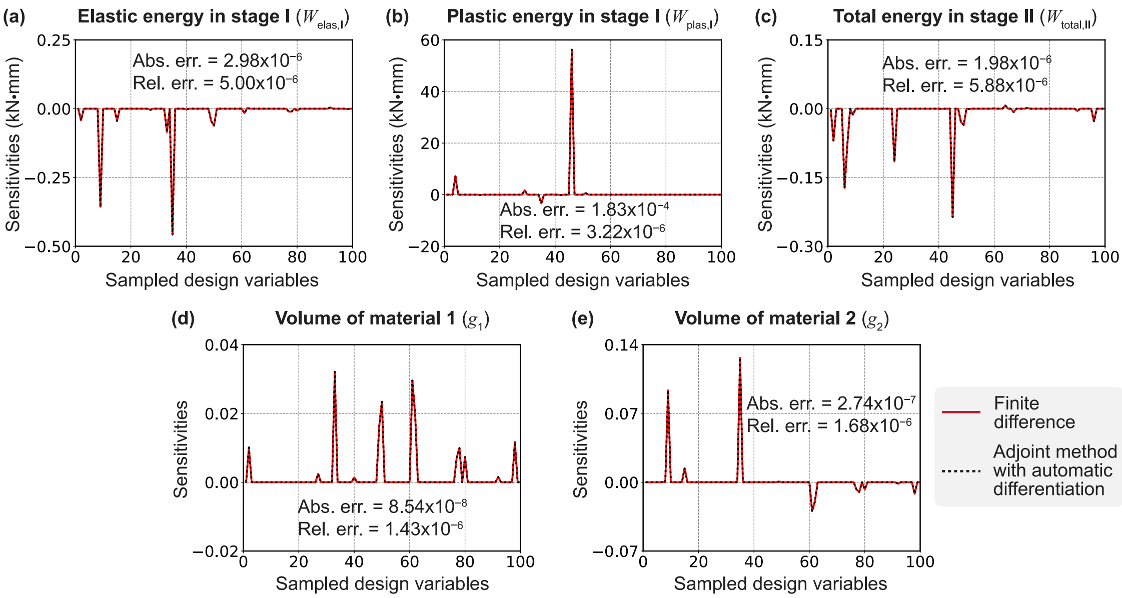

Fig. A.9. Comparisons of the sensitivities between the finite difference and the reversed adjoint method with automatic differentiation for various functions. (a) Elastic energy in stage I, $W_{\mathtt{elas,I}}$. (b) Plastic energy in stage I, $W_{\mathtt{plas,I}}$. (c) Total energy in stage II, $W_{\mathtt{total,II}}$. (d) Volume of material 1, g_1. (e) Volume of material 2, g_2.

Appendix B. Conversion from design variables to physical variables

In this section, we introduce the conversion from design variables (ρ and ξ_1–$\xi_{N^{\mathtt{mat}}-1}$) to physical variables ($\overline{\rho}$ and $\overline{\xi}_1$–$\overline{\xi}_{N^{\mathtt{mat}}}$) used in Section 3.1. Specifically, to alleviate the dependency of optimized designs on element size and avoid the checkerboard phenomenon caused by overestimated stiffness at mesh modes, we apply a linear filter (Bourdin, 2001) to the design variables. For a generic design variable, $\zeta \in \{\rho, \xi_1, \xi_2, \ldots, \xi_{N^{\mathtt{mat}}-1}\}$, we compute its filtered version ($\widetilde{\zeta} \in \{\widetilde{\rho}, \widetilde{\xi}_1, \widetilde{\xi}_2, \ldots, \widetilde{\xi}_{N^{\mathtt{mat}}-1}\}$) as

$$\widetilde{\zeta}(\mathbf{X}) = \frac{\displaystyle\int_{\Omega} w(\mathbf{X}, \mathbf{X}')\zeta(\mathbf{X}')\mathrm{d}\mathbf{X}'}{\displaystyle\int_{\Omega} w(\mathbf{X}, \mathbf{X}')\mathrm{d}\mathbf{X}'} \in [0, 1]$$

where $w(\mathbf{X}, \mathbf{X}') = \max\{0, R_{\zeta} - \|\mathbf{X} - \mathbf{X}'\|_2\}$ is a weighting factor determined by a prescribed filter radius, $R_{\zeta} \geq 0$, associated with the design variable, ζ. To derive a discrete design (0–1 solution for all design variables), we further apply the Heaviside projection (Bendsoe and Sigmund, 2003) to the filtered variables and yield the projected variables as

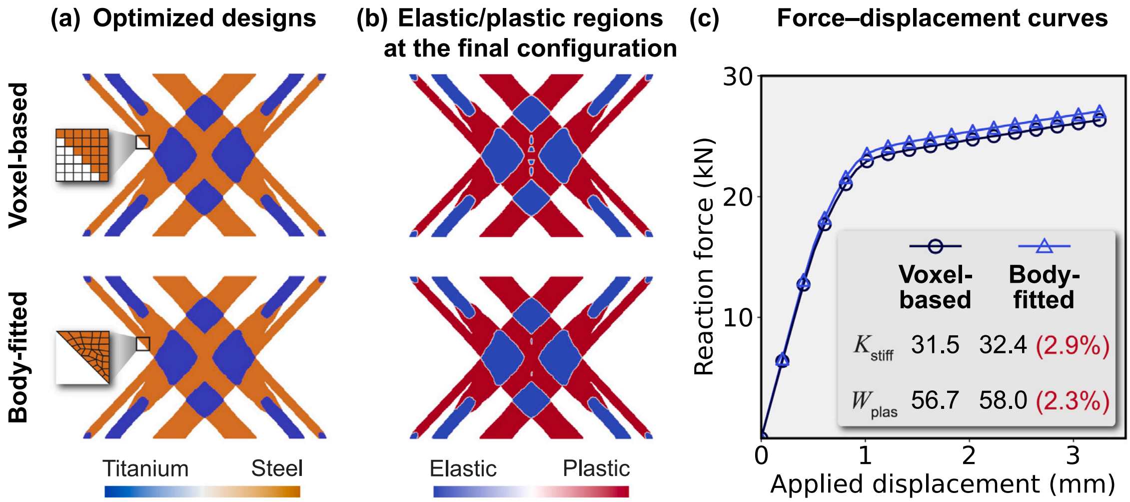

Fig. C.10. Comparisons of the (a) optimized designs, (b) elastic/plastic regions at the final configuration, and (c) force–displacement responses between the voxel-based and body-fitted meshes. The variables $K_{\mathtt{stiff}}$ and $W_{\mathtt{plas}}$ in (c) are initial stiffness (in kN/mm) and plastic energy (in kN·mm), respectively. The numbers in the parenthesis are the relative errors.

$$\hat{\zeta}(\mathbf{X}) = \frac{\tanh(\beta\theta) + \tanh(\beta(\tilde{\zeta}(\mathbf{X}) - \theta))}{\tanh(\beta\theta) + \tanh(\beta(1-\theta))} \in [0,1]$$

where $\hat{\zeta} \in \{\hat{\rho}, \hat{\xi}_1, \hat{\xi}_2, \ldots, \hat{\xi}_{N^{\mathtt{mat}}-1}\}$ represents a generic projected variable.

Upon Heaviside projection, we proceed with defining physical variables. Specifically, we define the physical density variable as $\bar{\rho} = \hat{\rho}$. We also define physical material variables, $\bar{\xi}_1(\mathbf{X})$, $\bar{\xi}_2(\mathbf{X})$, …, $\bar{\xi}_{N^{\mathtt{mat}}}(\mathbf{X}) \in [0,1]$, adhering to the equality constraint of $\sum_{n=1}^{N^{\mathtt{mat}}} \bar{\xi}_n = 1$. To efficiently enforce this constraint during topology optimization, we apply a modified version of the HSP in Zhou et al. (2018) to the projected material variables ($\hat{\xi}_1$–$\hat{\xi}_{N^{\mathtt{mat}}-1}$). The resulting physical material variables read as

$$\begin{cases} \bar{\xi}_n = \displaystyle\sum_{k=1}^{2^{N^{\mathtt{mat}}-1}} b_{nk} \left\{ (-1)^{N^{\mathtt{mat}}-1+\sum_{l=1}^{N^{\mathtt{mat}}-1} c_{kl}} \prod_{m=1}^{N^{\mathtt{mat}}-1} (\hat{\xi}_m + c_{km} - 1) \right\} \quad \text{for} \quad n = 1, 2, \ldots, N^{\mathtt{mat}} - 1 \\ \bar{\xi}_{N^{\mathtt{mat}}} = 1 - \displaystyle\sum_{n=1}^{N^{\mathtt{mat}}-1} \bar{\xi}_n \end{cases} \tag{B.1}$$

where the parameter $c_{kl} \in \{0,1\}$ is the lth coordinate component of the kth vertex of a unit hypercube in the $N^{\mathtt{mat}} - 1$ dimensional space. The parameter b_{nk} is computed as $b_{nk} = c_{nk} / \sum_l c_{nl}$ if $\sum_l c_{nl} \geq 1$ and $b_{nk} = 0$ otherwise.

Appendix C. Comparison between the voxel-based and body-fitted meshes

In Section 4, we conduct the numerical analysis using voxel-based (fixed-grid) meshes, which include both solid and void elements. This mesh type is commonly used in density-based topology optimization (Bendsøe and Kikuchi, 1988) for convenience. However, for manufacturing purposes, a body-fitted mesh that includes only the solid elements should be used. This section compares the elastoplastic responses of the optimized designs defined on voxel-based and body-fitted meshes.

Fig. C.10 provides a detailed comparative analysis based on Dsg. 3 from Fig. 5. According to Fig. C.10(a)–(b), the optimized designs defined on voxel-based and body-fitted meshes exhibit similar material distributions and elastic/plastic regions. Consequently, both designs produce consistent force–displacement responses as shown in Fig. C.10(c). In Fig. C.10(c), we also compute the initial stiffness ($K_{\mathtt{stiff}}$) and plastic energy ($W_{\mathtt{plas}}$) for the two designs. Comparing these values, we observe that the design defined on the body-fitted mesh shows negligible relative errors — 2.9% in $K_{\mathtt{stiff}}$ and 2.3% in $W_{\mathtt{plas}}$. Therefore, it is sufficient to use voxel-based meshes to design optimized elastoplastic structures.

Data availability

Data will be made available on request.

References

Abueidda, D.W., Kang, Z., Koric, S., James, K.A., Jasiuk, I.M., 2021. Topology optimization for three-dimensional elastoplastic architected materials using a path-dependent adjoint method. Internat. J. Numer. Methods Engrg. 122 (8), 1889–1910. http://dx.doi.org/10.1002/nme.6604.

Alberdi, R., Khandelwal, K., 2017. Topology optimization of pressure dependent elastoplastic energy absorbing structures with material damage constraints. Finite Elem. Anal. Des. 133, 42–61. http://dx.doi.org/10.1016/j.finel.2017.05.004.

Alberdi, R., Khandelwal, K., 2019a. Bi-material topology optimization for energy dissipation with inertia and material rate effects under finite deformations. Finite Elem. Anal. Des. 164, 18–41. http://dx.doi.org/10.1016/j.finel.2019.06.003.

Alberdi, R., Khandelwal, K., 2019b. Design of periodic elastoplastic energy dissipating microstructures. Struct. Multidiscip. Optim. 59, 461–483. http://dx.doi.org/10.1007/s00158-018-2076-2.

Alberdi, R., Zhang, G., Li, L., Khandelwal, K., 2018. A unified framework for nonlinear path-dependent sensitivity analysis in topology optimization. Internat. J. Numer. Methods Engrg. 115 (1), 1–56. http://dx.doi.org/10.1002/nme.5794.

Amir, O., 2017. Stress-constrained continuum topology optimization: A new approach based on elasto-plasticity. Struct. Multidiscip. Optim. 55, 1797–1818. http://dx.doi.org/10.1007/s00158-016-1618-8.

Baratta, I.A., Dean, J.P., Dokken, J.S., Habera, M., Hale, J.S., Richardson, C.N., Rognes, M.E., Scroggs, M.W., Sime, N., Wells, G.N., 2023. DOLFINx: The Next Generation FEniCS Problem Solving Environment. Zenodo, http://dx.doi.org/10.5281/zenodo.10447666.

Bendsøe, M.P., Kikuchi, N., 1988. Generating optimal topologies in structural design using a homogenization method. Comput. Methods Appl. Mech. Engrg. 71 (2), 197–224. http://dx.doi.org/10.1016/0045-7825(88)90086-2.

Bendsoe, M.P., Sigmund, O., 2003. Topology Optimization: Theory, Methods, and Applications. Springer Science & Business Media.

Boissier, M., Deaton, J.D., Beran, P.A., Vermaak, N., 2021. Elastoplastic topology optimization of cyclically loaded structures via direct methods for shakedown. Struct. Multidiscip. Optim. 64, 189–217. http://dx.doi.org/10.1007/s00158-021-02875-6.

Bourdin, B., 2001. Filters in topology optimization. Internat. J. Numer. Methods Engrg. 50 (9), 2143–2158. http://dx.doi.org/10.1002/nme.116.

Bradbury, J., Frostig, R., Hawkins, P., Johnson, M.J., Leary, C., Maclaurin, D., Necula, G., Paszke, A., VanderPlas, J., Wanderman-Milne, S., Zhang, Q., 2018. JAX: composable transformations of Python+NumPy programs.

Bruggi, M., 2008. On an alternative approach to stress constraints relaxation in topology optimization. Struct. Multidiscip. Optim. 36, 125–141. http://dx.doi.org/10.1007/s00158-007-0203-6.

Dalcín, L., Paz, R., Storti, M., 2005. MPI for Python. J. Parallel Distrib. Comput. 65 (9), 1108–1115. http://dx.doi.org/10.1016/j.jpdc.2005.03.010.

Desai, J., Allaire, G., Jouve, F., Mang, C., 2021. Topology optimization in quasi-static plasticity with hardening using a level-set method. Struct. Multidiscip. Optim. 64, 3163–3191. http://dx.doi.org/10.1007/s00158-021-03034-7.

Ferrari, F., Sigmund, O., 2020. A new generation 99 line Matlab code for compliance topology optimization and its extension to 3D. Struct. Multidiscip. Optim. 62, 2211–2228. http://dx.doi.org/10.1007/s00158-020-02629-w.

Gupta, R.K., Mathew, C., Ramkumar, P., 2015. Strain hardening in aerospace alloys. Front. Aerosp. Eng. 4 (1), 1–13.

Ivarsson, N., Wallin, M., Amir, O., Tortorelli, D.A., 2021. Plastic work constrained elastoplastic topology optimization. Internat. J. Numer. Methods Engrg. 122 (16), 4354–4377. http://dx.doi.org/10.1002/nme.6706.

Jia, J., Da, D., Hu, J., Yin, S., 2021. Crashworthiness design of periodic cellular structures using topology optimization. Compos. Struct. 271, 114164. http://dx.doi.org/10.1016/j.compstruct.2021.114164.

Jia, Y., Li, L., Wang, C., Lu, Z., Zhang, R., 2019. A novel shape memory alloy damping inerter for vibration mitigation. Smart Mater. Struct. 28 (11), 115002. http://dx.doi.org/10.1088/1361-665X/ab3dc8.

Jia, Y., Liu, K., Zhang, X.S., 2024a. Modulate stress distribution with bio-inspired irregular architected materials towards optimal tissue support. Nature Commun. 15, 4072. http://dx.doi.org/10.1038/s41467-024-47831-2.

Jia, Y., Liu, K., Zhang, X.S., 2024b. Topology optimization of irregular multiscale structures with tunable responses using a virtual growth rule. Comput. Methods Appl. Mech. Engrg. 425, 116864. http://dx.doi.org/10.1016/j.cma.2024.116864.

Jia, Y., Liu, K., Zhang, X.S., 2024c. Unstructured growth of irregular architectures for optimized metastructures. J. Mech. Phys. Solids 192, 105787. http://dx.doi.org/10.1016/j.jmps.2024.105787.

Jia, Y., Lopez-Pamies, O., Zhang, X.S., 2023. Controlling the fracture response of structures via topology optimization: From delaying fracture nucleation to maximizing toughness. J. Mech. Phys. Solids 173, 105227. http://dx.doi.org/10.1016/j.jmps.2023.105227.

Jia, Y.-Q., Wang, C., Li, L.-Z., Zhang, R.-F., Lu, Z.-D., 2022. Residual seismic performance of fire-damaged reinforced concrete frame structure with metallic yielding dampers. J. Struct. Eng. 148 (4), 04022003. http://dx.doi.org/10.1061/(ASCE)ST.1943-541X.0003284.

Jia, Y., Wang, C., Zhang, X.S., 2024d. FEniTop: A simple FEniCSx implementation for 2D and 3D topology optimization supporting parallel computing. Struct. Multidiscip. Optim. 67, 140. http://dx.doi.org/10.1007/s00158-024-03818-7.

Kim, S., Yun, G.J., 2020. Microstructure topology optimization by targeting prescribed nonlinear stress-strain relationships. Int. J. Plast. 128, 102684. http://dx.doi.org/10.1016/j.ijplas.2020.102684.

Krieg, R.D., Krieg, D.B., 1977. Accuracies of numerical solution methods for the elastic-perfectly plastic model. J. Press. Vessel. Technol. 99 (4), 510–515. http://dx.doi.org/10.1115/1.3454568.

Li, M., Deng, Y., Zhang, H., Wong, S.H.F., Mohamed, A., Zheng, Y., Gao, J., Yuen, T.Y.P., Dong, B., Kuang, J.S., 2021. Topology optimization of multi-material structures with elastoplastic strain hardening model. Struct. Multidiscip. Optim. 64, 1141–1160. http://dx.doi.org/10.1007/s00158-021-02905-3.

Li, W., Jia, Y., Wang, F., Sigmund, O., Zhang, X.S., 2023. Programming and physical realization of extreme three-dimensional responses of metastructures under large deformations. Internat. J. Engrg. Sci. 191, 103881. http://dx.doi.org/10.1016/j.ijengsci.2023.103881.

Li, W., Wang, F., Sigmund, O., Zhang, X.S., 2022. Digital synthesis of free-form multimaterial structures for realization of arbitrary programmed mechanical responses. Proc. Natl. Acad. Sci. 119, e2120563119. http://dx.doi.org/10.1073/pnas.2120563119.

Li, L., Zhang, G., Khandelwal, K., 2017. Topology optimization of energy absorbing structures with maximum damage constraint. Internat. J. Numer. Methods Engrg. 112 (7), 737–775. http://dx.doi.org/10.1002/nme.5531.

Margossian, C.C., 2019. A review of automatic differentiation and its efficient implementation. WIREs Data Min. Knowl. Discov. 9 (4), e1305. http://dx.doi.org/10.1002/widm.1305.

Maute, K., Schwarz, S., Ramm, E., 1998. Adaptive topology optimization of elastoplastic structures. Struct. Optim. 15, 81–91. http://dx.doi.org/10.1007/BF01278493.

Nakshatrala, P.B., Tortorelli, D.A., 2015. Topology optimization for effective energy propagation in rate-independent elastoplastic material systems. Comput. Methods Appl. Mech. Engrg. 295, 305–326. http://dx.doi.org/10.1016/j.cma.2015.05.004.

Paszke, A., Gross, S., Massa, F., Lerer, A., Bradbury, J., Chanan, G., Killeen, T., Lin, Z., Gimelshein, N., Antiga, L., Desmaison, A., Kopf, A., Yang, E., DeVito, Z., Raison, M., Tejani, A., Chilamkurthy, S., Steiner, B., Fang, L., Bai, J., Chintala, S., 2019. PyTorch: An imperative style, high-performance deep learning library. In: Advances in Neural Information Processing Systems, 32, Curran Associates, Inc..

Prager, W., 1955. The theory of plasticity: A survey of recent achievements. Proc. Inst. Mech. Eng. 169 (1), 41–57. http://dx.doi.org/10.1243/PIME_PROC_1955_169_015_02.

Simo, J.C., Hughes, T.J., 2006. Computational Inelasticity, vol. 7, Springer Science & Business Media.

Simo, J.C., Taylor, R.L., 1986. A return mapping algorithm for plane stress elastoplasticity. Internat. J. Numer. Methods Engrg. 22 (3), 649–670. http://dx.doi.org/10.1002/nme.1620220310.

Svanberg, K., 1987. The method of moving asymptotes—a new method for structural optimization. Internat. J. Numer. Methods Engrg. 24 (2), 359–373. http://dx.doi.org/10.1002/nme.1620240207.

Talischi, C., Paulino, G.H., Pereira, A., Menezes, I.F.M., 2012. PolyTop: A Matlab implementation of a general topology optimization framework using unstructured polygonal finite element meshes. Struct. Multidiscip. Optim. 45, 329–357. http://dx.doi.org/10.1007/s00158-011-0696-x.

Wallin, M., Jönsson, V., Wingren, E., 2016. Topology optimization based on finite strain plasticity. Struct. Multidiscip. Optim. 54, 783–793. http://dx.doi.org/10.1007/s00158-016-1435-0.

Wang, C., Zhao, Z., Zhou, M., Sigmund, O., Zhang, X.S., 2021. A comprehensive review of educational articles on structural and multidisciplinary optimization. Struct. Multidiscip. Optim. 64, 2827–2880. http://dx.doi.org/10.1007/s00158-021-03050-7.

Wei, C., Liu, L., Cao, H., Zhong, X., Xu, X., Gu, Y., Cheng, D., Huang, Y., Li, Z., Guo, W., Liu, Z., Li, L., 2022. Cu10Sn to Ti6Al4V bonding mechanisms in laser-based powder bed fusion multiple material additive manufacturing with different build strategies. Addit. Manuf. 51, 102588. http://dx.doi.org/10.1016/j.addma.2021.102588.

Wei, C., Zhang, Z., Cheng, D., Sun, Z., Zhu, M., Li, L., 2020. An overview of laser-based multiple metallic material additive manufacturing: From macro- to micro-scales. Int. J. Extrem. Manuf. 3 (1), 012003. http://dx.doi.org/10.1088/2631-7990/abce04.

Zhang, X., Li, X., Zhang, Y., 2023. A framework for plasticity-based topology optimization of continuum structures. Internat. J. Numer. Methods Engrg. 124 (7), 1493–1509. http://dx.doi.org/10.1002/nme.7172.

Zhang, R., Wang, C., Pan, C., Shen, H., Ge, Q., Zhang, L., 2018. Simplified design of elastoplastic structures with metallic yielding dampers based on the concept of uniform damping ratio. Eng. Struct. 176, 734–745. http://dx.doi.org/10.1016/j.engstruct.2018.09.009.

Zhou, Y., Nomura, T., Saitou, K., 2018. Multi-component topology and material orientation design of composite structures (MTO-C). Comput. Methods Appl. Mech. Engrg. 342, 438–457. http://dx.doi.org/10.1016/j.cma.2018.07.039.